Title
Using Solution Phase Self-Assembly to Control the Properties of Magnetic and Magnetoelectric Nanostructures

Author
Schelhas, Laura Theresa

Publication Date
2013

Peer reviewed|Thesis/dissertation

UNIVERSITY OF CALIFORNIA

Los Angeles

Using Solution Phase Self-Assembly to Control the Properties of Magnetic and Magnetoelectric Nanostructures

A dissertation submitted in partial satisfaction of the requirements

for the degree Doctor of Philosophy in Chemistry

by

Laura Theresa Schelhas

2013

ABSTRACT OF THE DISSERTATION

Using Solution Phase Self-Assembly to Control the Properties of Magnetic and Magnetoelectric Nanostructures

by

Laura Theresa Schelhas

Doctor of Philosophy in Chemistry

University of California, Los Angeles, 2013

Professor Sarah H. Tolbert, Chair

Nanostrutured magnetic materials have gained much recent interest because of their application in various electronic systems. These materials, however, often require complex lithography and epitaxy to control the magnetic properties. In this work, solution-phase self-assembly is used to create magnetic and magnetoelectric materials with a variety of nanoscale structures. By engineering the architecture of the system, control over a range of magnetic properties can be realized.

The first part of this work focuses on nano-magnetic materials. Here, the organization of nanoscale magnets into different geometries is controlled, and the properties of the systems are studied. In the first chapter, Ni-Cu nanowire stacks are examined to explore the effect of shape anisotropy on the coupling between different elements. This work provides insight into how to design new elements for spin-torque devices. In the next chapter, directed self-assembly of

block copolymers is used to create coupled 1D chains of ferromagnetic and superparamagnetic FePt nanoparticles. These nano-patterned are globally aligned on the wafer length-scale using micron-sized lithographic grooves. This system is ideal for studying dipolar coupling between magnetic nanocrystals. Additionally, the processing methods developed here provide a platform for organizing other types of nanomaterials.

The second sections explore magnetoelectric materials. These are materials that combine ferromagnetism and ferroelectricity in a coupled manner. One material that does this intrinsically is bismuth ferrite. The first chapter of this section explores ordered nanoporous bismuth ferrite produced by block copolymer templating. It is shown that the ordered porosity of the system creates a unique strain state in the bismuth ferrite, which in turn produces a large change in magnetization upon application of an electric field. Finally, in the last chapter, a nanostructured composite magnetoelectric system is studied. Here, magnetostrictive Ni nanocrystals are coupled to a single-crystalline piezoelectric substrate. The nanocrystals are superparamagnetic and show no net magnetization. Upon application of an electric field, however, strain induced in the piezoelectric substrate strains the lattice of the nanocrystals, creating a preferred magnetic axis along the high strained direction. This locks the magnetization along the strain axis and switches the nanocrystals from a superparamagnetic to a ferromagnetic state.

This dissertation of Laura Theresa Schelhas is approved.

Kang L. Wang

Xiangfeng Duan

Sarah H. Tolbert, Committee Chair

University of California, Los Angles

2013

To everyone who believed I could do this when I did not believe it myself.

TABLE OF CONTENTS

LIST OF FIGURES

CHAPTER 2. Magnetic Confinement and Coupling in Narrow-Diameter Au-Ni Nanowires

LIST OF SCHEMES

LIST OF TABLES

ACKNOWLEDGEMENTS

I first would like to thank my family who, however reluctantly, supported my decision to move clear across the country to pursue a further degree in chemistry. It was not an easy adventure and had many ups and downs but they stood with me and supported me through it all. I would like to specifically thank my parents Rick and Pam for their visits and shopping trips over the years. Parents know it is important to stay well feed when working hard. I also wish to thank my Grammy Jackie and Grandpa Butch for making the long trip out to see my graduation. I am certain that Pinball Grandma and Grandpa would be happy to know that not a day goes by that I don't think about the influence they had on my life and I wish I could share this with them. Mike Thompson thank you for being my strongest support system. You have had to deal with my moods and frustrations more than anyone else but you have stood with me through all of it; thank you and I love you. Finally I would like to acknowledge Daisy and Chloe for being the best and most entertaining kitties I could ask for they have provided much needed cuddles and companionship throughout this process.

I have had the privilege to work with Professor Tolbert over the past years. Sarah has been probably the biggest influence in turning me into the scientist I am today. I started this program with little confidence and had a huge fear of speaking. Sarah taught me the skills I needed to do quality research as well as the skills and confidence I needed to be able to tell people about the work I do. I greatly appreciate how easy it was to talk to Sarah not only about science but a number of things. By the end of this work I felt like we worked as a team to complete much of this work and I appreciate not only the opportunity to learn from her but to learn with her. I cannot thank Sarah enough for her support and belief in me.

I also acknowledge all the support I have received from all the past and current members of the Tolbert group. I truly believe one of the biggest support systems you have during graduate school is your lab and officemates and I think I had some of the best. There is never a quite moment in the offices and there are many found memories with all of you. I would also like to acknowledge my collaborators in the Carman Lab. They have also provided many hours of entertainment as well as very useful scientific discussion.

Rachel Huber and Amy Ferreira deserve a special thank you. I also want to thank Dr. Courtney Sorrell (Richman) even if your time with us was short you made a large impact. They have been my closest team in the Tolbert group; reading everything I throw at them and listening to my countless ramblings about magnets and really any other strange things that come out of my mouth. I will always appreciate our walks and long lunches. Thank you girls for all of your help.

Dr. Richie Farrell, I thank you for teaching me how to work efficiently. You showed me how much time I can save by keeping myself organized. Richie, you were also able to get me excited about the projects we worked on. I also wish to thank Dr. Tom Quickel. Tom you were always willing to answer any questions no matter how foolish. I also loved how you were always armed with an awesome and adorable kitten video if anyone needed cheering up. I had fun with you both on our countless trips to SSRL. Many sleepless hours made for some interesting and fun experiences. Abraham Buditama, you became my SSRL buddy when Tom and Richie were gone and those are some times I will never forget. I think it takes a special person to understand the fun we had at 7-2 and I don't think anyone will ever be able to top our diffraction interpretive dance.

I want to acknowledge all of my collaborators as well. Professor Carman has had a huge influence on my research. I appreciate his enthusiasm for his work and his willingness to give

me useful advice and I will never forget some of his stories. I wish to specially thank his group members that have provided the most assistance: Dr. Hyungsuk Kim (Thank you so much!!), Dr. Josh Hockel, Dr. Scott Keller, Kyle Wetzlar, Paul Nordeen, Wei Sun, and Scott Strutner. Professor Jane Chang has also been a wonderful collaborator and I want to thank the members of her group, mainly Diana Chen and Calvin Pham for the time and effort they have provided in our collaboration.

There have been a number of important people that have helped me as well that I truly couldn't have done half of this work without them. First is Dr. Ignacio Martini. Ignacio thank you for all of your help with SQuID, XPS, and SEM. Your knowledge of instrumentation was a huge inspiration for me to really understand what I was doing. Because of the difficult questions you asked it lead me to a greater understanding of my research and I cannot thank you enough for that. I also have to thank the beamline scientists at SSRL for providing scientific support. I would like to specifically thank Ron Marks, Doug Van Campen, and Chad Miller. Thank you all for teaching me and inspiring me.

I wish to thank my committee members, Professors Kang L. Wang, and Xiangfeng Duan for their help and support in writing this thesis. I also wish to thank Professor William Gelbart for serving on my oral committee and always have a smile for me while waiting to talk to Sarah. Finally I would like to acknowledge Dean Jane Chang and Professor Carman for providing letters of recommendation.

Previous Publications and Contributions of Co-Authors

Chapter 2 is a version of: Laura T. Schelhas, Matthew J. Banholzer, Chad A. Mirkin, Sarah H. Tolbert, "Magnetic Confinement and Coupling in Narrow-Diameter Au-Ni Nanowires." Matthew prepared the samples and performed the SEM analysis of the samples. We worked

together on the writing of the manuscript and Professor Mirkin and Professor Tolbert both helped edit the manuscript. This manuscript will be submitted for publication shortly after this dissertation is filed.

Chapter 3 is a version of: Laura T. Schelhas, Richard A. Farrell, Sarah H. Tolbert, "Directed Self-Assembly as a route to Ferromagnetic and Superparamagnetic Nanoparticle Arrays." Richard helped with all the initial sample fabrication and optimization. I wrote most of the manuscript and Professor Tolbert and Richard helped edit the manuscript. This manuscript will be submitted for publication shortly after this dissertation is filed.

Chapter 4 is a version of: Thomas E. Quickel, Laura T. Schelhas, Richard A. Farrell, Nikolay Petkov, Van H. Le, Sarah H. Tolbert, "Mesoporous Bismuth Ferrite with Electric Field Amplified Ferromagnetism." Van helped with the initial synthesis of the materials. Nikolay helped with the STEM of the nickel plated BFO. Richard helped with all the magnetic and high-resolution x-ray measurements. Thomas and I contributed equally the to writing of the manuscript and Professor Tolbert helped edit the manuscript. This manuscript will be submitted for publication shortly after this dissertation is filed.

Chapter 5 is a version of: Hyungsuk K.D. Kim, Laura T. Schelhas, Scott Keller, Joshua L. Hockel, Sarah H. Tolbert, Gregory P. Carman, "Magnetoelectric Control of Superparamagnetism." *Nano Letters,* 2013, 13, 3 (884-888). Scott helped with the theoretical calculations. Joshua helped with the strain measurements. Hyungsuk and I contributed equally to the work in this paper as well as writing the manuscript. Professor Tolbert and Professor Carman helped edit the manuscript.

Professor Sarah Tolbert directed the research presented in this manuscript. This work was supported by: National Science Foundation (NSF); WIN center (funded by UC Discovery

Program, Intel, and the NERC); Translations Application for Nanoscale Applications (TANMS); University of California, Los Angeles dissertation year fellowship; California NanoSystem Institute (CNSI); and University of California, Los Angeles Graduate Division. Portions of this research were performed at the Stanford Synchrotron Radiation Light Source, a national user facility operated by Stanford University on behalf of the U.S. Department of Energy, Office of Basic Energy Science.

VITA

2007	B.S. in Chemistry, Michigan State University
2007 – 2012	Teaching Assistant, Department of Chemistry and Biochemistry UCLA
2008	Excellence in Teaching, Department of Chemistry and Biochemistry, UCLA
2009	Best Presentation Award, Nanotechnology Student Summer School, NIMS/MANA (Japan), Nanoscience Centre, University of Cambridge (UK), UCLA/CNSI (USA)
2010 – 2013	PEERS Chemistry Workshop Facilitator, UCLA
2011	California Nanosystems Institute, High School Nanoscience Program, UCLA
2012	Departmental Travel Grant for ACS meeting, March 2012, Department of Chemistry and Biochemistry, UCLA
2012	American Chemical Society Travel Award Fellowship, ACS Meeting March 2012
2012 – 2013	Dissertation Year Fellowship, UCLA
2012 – 2013	NSF ERC – Translational Application of Nanoscale Multiferroic Systems (TANMS), Student Leadership Council President
2013	MMM/Intermag Conference Student Travel Award, Chicago 2013
2013	Best Poster Presentation: TANMS Annual Review, UCLA

PUBLICATIONS AND SELECTED PRESENTATIONS

L. T. Schelhas, H. Kim, J. Hockel, S. Keller, S. H. Tolbert, G. P. Carman, 12th Joint MMM/Intermag Conference, Chicago, IL, Jan 14 – 18, 2013. Oral Presentation: Magnetoelectric Control of the Superparamagnetic Limit.

L. T. Schelhas, H. Kim, J. Hockel, S. Keller, S. H. Tolbert, G. P. Carman, "Magnetoelectric Control of the Superparamagnetic Limit" *Nano Letters,* 2013 *13* (3), 884-888.

I. E. Rauda, L.C. Saldarriaga-Lopez, Helms, B.A., **L. T. Schelhas**, D. Membreno, D.J. Milliron, S. H. Tolbert, "Nanoporous Semiconductors Synthesized Through Polymer Templating of Ligand-Stripped CdSe Nanocrystals" *Advanced Materials*, 2013 *25* (9), 1315-1322.

I. E. Rauda, R. Buonsanti, L. C. Saldarriaga-Lopez, K. Benjauthrit, **L. T. Schelhas**, M. Stefik, V. Augustyn, J. Ko, B. Dunn, U. Wiesner, D. J. Milliron, S. H. Tolbert "General Method for the Synthesis of Hierarchical Nanocrystal-Based Mesoporous Materials" *ACS Nano* 2012 *6* (7), 6386-6399.

L. T. Schelhas, R. Farrell, S. H. Tolbert 243rd ACS National Meeting & Exposition, San Diego, CA March 25- 29 2012. Oral Presentation: 1D Ferromagnetic Nanoparticle Arrays Using Block Copolymer Directed Self-Assembly.

L. T. Schelhas, M. J. Banholzer, C. A. Mirkin, S. H. Tolbert Nanotechnology Student Summer School, The 6th NIMS/MANA(Japan), Nanoscience Centre, Univeristy of Cambridge (UK), UCLA/CNSI (USA) Nanotechnology Students' Summer School, Los Angeles, CA July 27-31, 2009. Oral Presentation: Magnetic Shape Anisotropy in Nanoscale Ni-Disks and Rods.

L. T. Schelhas, J. Shane, M. Dantus "Advantages of ultrashort phase-shaped pulses for selective two-photon activation and biomedical imaging" *Nanomedicine-Nanotechnology Biology and Medicine* 2006, *2*, 177-181.

CHAPTER 1

Introduction

Magnetic materials have been known to have application in a variety of electronic systems. In addition to magnetic materials, magnetoelectric materials have also gained considerable attention. An example of this is the large amount of research currently being done to study memory and data storage.[1] Memory devices can utilize a variety of different methods to control magnetism. One option is the application of magnetic fields, but it can be very difficult to apply a magnetic field in a device. Heat assisted memory takes advantage of the fact that magnetism is temperature dependent; however, application of additional heat in electronics has its own set of problems.[2] Another form of memory is magnetoelectric memory devices.[3] These devices combine magnetic materials with the ability to tune that magnetism using an electric field. In more traditional devices, current is passed creating large amounts of resistance and heat loss[4]; these systems therefore do not scale down to the small scale very efficiently. By using electric field, no current is passed creating much more efficient devices.

By creating new nanomaterials by less expensive wet chemical methods we have developed materials with exciting magnetic and electronic properties. By making nanostructured materials we can create magnetic domains and control how they interact though strain and electric fields.[5–7] Changing the nanostructure of different materials allows us to control the magnetic properties without having to apply a magnetic field, which can be difficult to do in a device.

An interesting class of materials I study are magnetoelectric materials. These are a type of multiferroic material, which combines ferromagnetism and ferroelectricity in a single material, allowing control of one parameter through the other.[8] Ferroelectricity is when a material possesses a spontaneous electric dipole. Similarly ferromagnetism is when a material possesses a permanent magnetic dipole. Few materials achieve this intrinsically, where both of these properties are present in a single material. At low temperatures a class of materials that gain ferroelectricity through magnetic ordering has been discovered.[9] These effects arise from symmetry breaking of very complex magnetic order; however, these materials require large fields and very low temperatures in order for these effects to be present. For these reasons they are not very useful for application in devices. There does exist a material, bismuth ferrite (BFO), that is multiferroic at room temperature and for this reason it is one of the most widely researched examples of a multiferroic material.[10–12] Additionally another class of multiferroic materials known a hexaferrites, due to their hexagonal crystal structure, has recently been gaining attention since they do have magnetoelectric properties at room temperature.[13] These materials are also interesting as their synthesis is similar to the BFO system and can lead to future applications of the architectures shown herein.[14]

Other routes to magnetoelectric materials involve coupling together a piezoelectric phase material such as lead magnesium niobate lead titante, (PMN-PT) with a magnetostrictive magnetic phase, such as nickel.[6,7] Piezoelectic materials create an electric field upon mechanical strain. Magnetostrictive materials deform in its shape upon application of a magnetic field. In such composites the reverse of these two properties is used; the piezoelectric phase produces a strain, which modifies the magnetic easy access, or preferred magnetic orientation, of the

magnetic phase. Magnetoelectric control in materials allows for control of magnetic properties by applying electric fields rather than the more difficult application of magnetic fields.

This work focuses on the general topic of using nanoscale architecture to control various properties in magnetic materials. I am specifically examining the use of solution-phase self-assembly and wet chemistry as a new method to reach the end goal of using nanomagnets in logic and data storage. Specific projects include the use of electrochemically deposited metal discs and rods for use as the free layer in spin torque devices, coupled quantum dots arrays for spin based signal processing, and nanostructured magnetoelectric materials. Within magnetoelectrics, I have focused on tuning the properties of intrinsic magnetoelectrics using strain, and on coupling magnetic nanocrystals to bulk piezoelectric substrates to make materials where magnetism can be turned on and off with strain.

My research is divided into four chapters: (Chapter 2) spin-torque systems, (Chapter 3) 1D nanoparticle arrays of magnetic nanoparticles, (Chapter 4) the effect of nanoscale architecture on magnetoelectric materials, and (Chapter 5) the use of magnetoelectric coupling to control the superparamagnetic limit of Ni nanoparticles.

The first part of this work focuses on the organization of different nanoscale magnetic geometries. This work focuses on the magnetic coupling of these systems in various architectures. In chapter 2 using Ni-Cu nanowire stacks we have explored potential new geometries for spin-torque devices, which is an exciting type of magnetically controlled resistive switch. These stacks are created by reproducible and tunable electrochemical deposition into anodic alumina templates. By combining magnetic disk shaped segments with rod shapes we propose a possible hybrid structure for the “free layer” in a spin-torque device. The orthogonal relationship between the magnetic easy axis of the disk and rod geometries creates a 3-state

magnetic system (e.g. right, left, and up) where the relative magnitude of the easy axes can be tuned by varying the size of the non-magnetic spacer layer between each disk-rod pair. This coupled system may lower the energy needed to write information in a spin-torque device.

In chapter 3, by using directed self-assembly of block copolymers, coupled 1D chains of ferromagnetic and superparamagnetic FePt nanoparticles are aligned within block copolymer nanopatterns. This solution-phase polymer templating approach can produce patterned arrays of magnetic nanoparticles with critical dimensions below those of conventional lithography. Physical-epitaxy is used to align polystyrene-block-polydimethylsiloxane (PS-b-PDMS). After removal of the PS block via reactive-ion etching, atomic layer deposition (ALD) of alumina is used to reduce the spacer between PDMS lines. This allows for tuning of the channel dimensions with angstrom level accuracy. We can then control the geometry of the nanoparticles in the channels; specifically in this system one dimensional chains. The coupling of nanoparticles is investigated using SQuID magnetometery.

The next part of this work focuses on magnetoelectric systems. In chapter 4, using solution-phase self-assembly of block copolymers (BCP) and inorganic precursors we have been able to create mesoporous versions of the intrinsic magnetoelectric material $BiFeO_3$, (BFO). Here it is shown that porosity and the mechanical flexibility that accompanies that porosity leads to interesting and exciting new properties. In this work the effects of electrical poling on the overall magnetic moment (M_s) for mesoporous and dense BFO. SQuID measurements show dense films exhibit little change in M_s upon electrical poling, while mesoporous BFO shows an increase from 0.01 to 0.94 m_b/Fe; currently the highest recorded value for BFO films. Based on *in-situ* diffraction, we find that the pore flexibility induces a strain anisotropy into the film, which in turn leads to increased spin canting upon electrical poling.

Next we explore a composite magnetoelectric system. In chapter 5 we use an electric field-induced strain from a piezoelectric PMN-PT substrate to strain superparamagnetic Ni nanoparticles. The small nanocrystals show no net magnetism because the magnetic dipole can rapidly fluctuate between easy axes, given the available thermal energy at room temperature, which is the defined as superparamagnetism. By straining the crystalline lattice of the nanocrystals, we can lock the magnetism along the strain axis and switch the nanocrystals between ferromagnetic and superparamagnetic states. We are able to show that there is an induced shift in the blocking temperature (the temperature where spins go from pinned to free) upon electrical poling. By controlling the blocking temperature of the material, we are able to tune the magnetic properties of the Ni nanoparticles without adding any heat to the system. This electric control over superparamagnetism can help reduce the currents needed during the writing process in memory devices.

Chapter 6 summarizes the scope of this work as well as future directions of this research. Finally an appendix is included to describe detailed synthetic conditions for the materials described in this work as well as details on SQuID magnetometry and XPS analysis.

Overall, the purpose of this work is to show that through careful control of nanoscale architecture the magnetic and magnetoelectric properties of various materials can be tuned and controlled.

CHAPTER 2

Magnetic Confinement and Coupling in Narrow-Diameter Au-Ni Nanowires

2.1 Introduction

The ability to organize magnetic and nonmagnetic materials across different length scales has led to the synthesis of devices that show novel magnetic effects.[15,16] Magnetoresistive spin-valves are a common example, where spin transfer between layers of magnetic materials can result in changes in the electrical resistance of the material.[15,16] In spin-valve devices, resistance is dependent on the relative spin orientation of two separated magnetic layers. The first magnetic layer, the free layer, can switch between magnetic oriented, while the second layer, the pinned layer, contains spins that are oriented in a fixed direction. These two magnetic layers are separated by a nonmagnetic spacer layer.[17] Parallel spins in the two magnetic regions allow for low device resistance to an injected spin-polarized current, while antiparallel spins produce a high resistance this effect is known as giant magnetoresistance (GMR).[16,18,19]

Previous work has built on the basic geometry described above by utilizing a perpendiculat spin polarizer.[20–24] The polarizer allows for a more energy efficient out-of-plane switching of the magnetic spin as opposed to the less favorable in-plane switching. There have been large scale demonstrations of the composite geometry(~100x200 nm^2) prepared by lithography. [21,25]

2.2. Experimental

In our system we prepare via electrochemical methods small scale (~50 nm) disk/rod coupled system to study this effect. In this fundamental study we vary the spacer distance

between the disk and rod to study the effects on the coupling between the two magnetic components. It is worthwhile to note that previous work has made measurements on electroplated multilayer systems that have shown .[26–28] These effects are not large; therefore, these would not be used as actual devices. However, this study shows that electrodeposition can be used to very accurately and reproducibly tune the geometry of the materials making it an ideal system for a fundamental study of the coupling of various sample geometries.

Magnetic nanowires were synthesized in a similar manner to previously published work.[29–32] Circular sheets of AAO (13 mm) with 45 nm inner diameter pores were purchased from Synkera Inc. and used as templates for the rod synthesis (note that the labeled pore size on the AAO used here was 35 nm, but significant variation is observed). Ag (200 nm) was evaporated on one side of each template and used as a working electrode to deposit the rod materials. The templates were mounted into an electrochemical cell, and 2 C of an Ag "buffer" layer was deposited under constant potential electrolysis at -1150 mV (Technic Inc. 1025 RTU plating solution diluted to 80% concentration was used). The electrochemical cell was thoroughly rinsed, and Au and Ni sections were alternately plated (at -970 and -910 mV, employing Technic Inc Orotemp 24 Rack and Nickel Sulfamate RTU solutions, respectively) until the desired nanowire segment lengths were achieved. The Ag backing/buffer layer was then etched in a 3:1:1 mixture of 95% ethanol to 30% H_2O_2 (in H_2O) to 28% NH_4OH (in H_2O). The alumina network was further etched off a small portion of each sample and the freed nanowires were examined in a Hitachi 4800 SEM (Fig. 2.1). The remainder of the wires remained within the alumina membrane for magnetic characterization. M-H curves were measured by SQUID Magnetometry using a Quantum Design MPMS with DC detection. Samples were measured with the field applied parallel and perpendicular to the pore long axis. A TJA Radial Iris 1000 ICP-

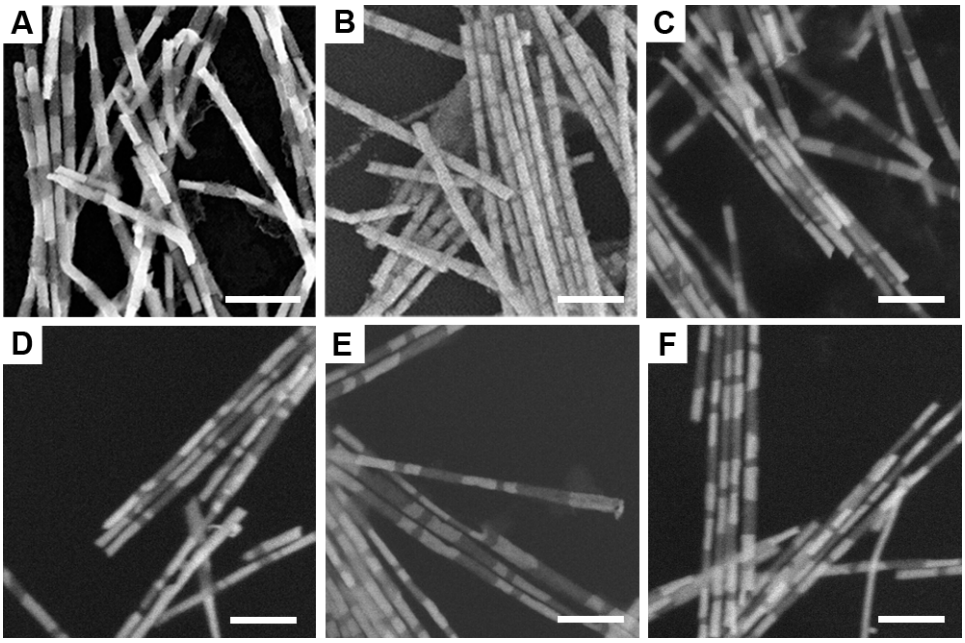

Figure 2.1. Selected SEM images of nanorods used in study. (A) 153 nm long Ni rods separated by 155 nm Au segments, diameter = 48 nm (B) 19 nm long Ni disks separated by 143 nm Au segments, diameter = 45 nm (C) Pairs of 148 nm long Ni segments and 26 nm long Ni segments separated by 11 nm Au segments. (D) Pairs of 161 nm long Ni segments and 30 nm long Ni segments separated by 29 nm Au segments. (E) Pairs of 168 nm long Ni segments and 32 nm long Ni segments separated by 52 nm Au segments. (F) Pairs of 168 nm long Ni segments and 31 nm long Ni segments separated by 124 nm Au segments. In (C-F), each Ni-rod Au-spacer Ni-disk pair is separated by approximately 140 nm of Au. Scale bars are 300 nm in all cases.

OES was used to determine the relative concentrations of Ni in the coupled wires. This allowed us to subtract out the magnetic contribution of the rods in coupled rod-disk systems. Samples for ICP-OES were digested in 300 µl of Optima HCl and 100 µl of Optima HNO_3 and diluted with 8 ml of 5% Optima HNO_3 after 3 hours heating at 85ºC.

2.3 Results and Discussion

The shape of magnetic materials plays an important role in determining the overall magnetic properties. This is most prominently manifested in nanosystems as these are frequently single domain magnets. Typically, the long axis of a nanostructure provides the more energetically favorable orientation for spin alignment; this is commonly named the easy magnetic axis. The origin of this effect occurs when magnetic charges or poles at the surface of the material create a magnetic field that acts to oppose the internal magnetization of the sample.[15] This demagnetizing field is dependent on the shape of a nanostructure; as the aspect ratio increases, this demagnetization factor along the long axis approaches zero. Since the demagnetization factor is inversely proportional to ease of magnetization, it becomes easier to magnetize the sample in the long direction, thus creating the easy axis. Note that this shape anisotropy is distinct from magnetocrystalline anisotropy, which arises from bond anisotropy within the crystal lattice.[15] While both are present in magnetic nanosystems, shape anisotropy generally dominates over magnetocrystalline anisotropy.[15] In our system, we deliberately synthesized rods and disks (aspect ratio >3:1 and <1:2, respectively) that should exhibit complementary easy axes: along the long axis of the rod structure or in the plane of the disk.

Nanostructures of varying aspect ratios were synthesized with the goal of finding structures that showed the highest magnetic anisotropy (i.e. high remanence and coercivity in

only one axis) (Fig. 2.1). The easy magnetic axis of the high aspect ratio rods and low aspect ratio disks were identified by examining hysteresis loops in M-H curves. An example of a hysteresis loop for an optimized rod sample is shown in figure 2.2A. These data indicate a single magnetic easy axis along the long axis of the rod, as shown by a high remanence (0.936) and coercivity (1660 Oe) when the magnetic field is applied parallel to the long axis of the rod. Conversely when the magnetic field is applied perpendicular to the long axis of the rod, both remanence (0.071) and coercivity (240 Oe) are low. Alternatively, disk segments exhibit a planar distribution of easy axes within the plane of the disk (Fig 2.2B). This is evidenced by a larger remanence when the magnetic field is applied parallel to the plane of the disk (0.541) rather than when applied perpendicular to the plane of the disk (0.293). While the anisotropy is much weaker in disk segments compared to the rod structures, this result is consistent with previous findings concerning magnetic shape anisotropy of similar structures.[33–36]

In determining these optimized aspect ratios, a range of disk and rod samples were examined. Table 2.1 summarizes the magnetic anisotropy measured for 5 particularly illustrative samples, 3 rods and 2 disks. The table shows aspect ratio, absolute length or thickness, and the ratio of remanent magnetization along the easy magnetic axis compared to the remanence in the hard direction. For rod-like structures, this is a ratio of the remanence parallel to the long axis of the rod divided by the remanence perpendicular to the rod. For disks, the opposite ratio is used – the table reports the remanence parallel to the plane of the disk divided by the remanence perpendicular to the plane of the disk. Defined in this way, the highest ratio always indicates the most ideal structure. For rod like structures, an aspect ratio of 2:1 produces modest anisotropy, but the anisotropy increases significantly when the aspect ratio increases to 3:1 or higher. Samples similar to R2 were thus used as the rod-like segment in all work on coupled structures.

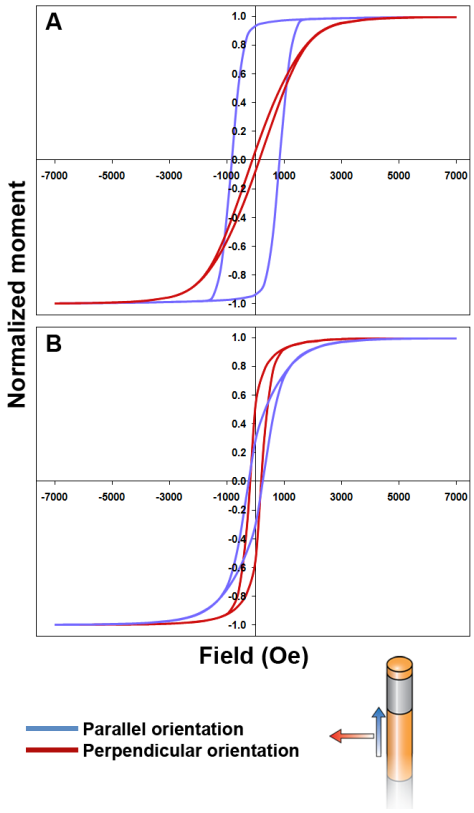

Figure 2.2. Magnetic response curves obtained on 153 nm long Ni rods and 19 nm thick Ni disks, both created in pores 45 nm in diameter. (A) High aspect ratio rods aligned parallel to the applied magnetic field exhibit a coercivity of 1660 Oe and a remanence of 0.936. Under perpendicular magnetization these rods exhibit a coercivity of only 240 Oe and a remanence of 0.071. (B) Low aspect ratio disks with the plane of the disk orientation parallel to the applied magnetic field (and thus the pore axis perpendicular to the field) exhibit coercivity of 390 Oe and remanence of 0.541. When the applied filed is parallel to the pore axis (perpendicular to the plane of the disk), the coercivity is 480 Oe and the remanence is only 0.293. This implies an easy axis that lies in the plane of the disks. The bottom of the figure contains are cartoon illustrating parallel and perpendicular magnetic fields.

Table 2.1. Effects of aspect ratio on magnetic anisotropy

Rods	Aspect Ratio	Length (nm)	M_r length / M_r diameter
R1	2.0	70	3.7
R2	3.2	153	13.4
R3	4.0	1330	0.8
Disks	Aspect Ratio	Length (nm)	M_r diameter / M_r thickness
D1	0.2	8	0.8
D2	0.4	19	1.9

When the dimensions get to be too large – either too long or too wide and too long, as seen in R3 – the remanent anisotropy plummets because the rods no longer contain a single magnetic domain and shape anisotropy no longer dominates the domain alignment. For disks, we expected that thinner structures would be better, but comparison of samples D1 and D2 indicates that the disks can be too thin. This likely stems from roughness within the nanowire stack. While our method can be used to precisely plate a desired thickness of metal, if the nucleating surface is not flat, the resulting disk-like structure will not be perfectly flat. Shapes that are thick compared to the roughness thus show higher magnetic anisotropy. Samples similar to D2 were thus used as the disk-like segment in all work on coupled structures.

As previously stated, the components of a spin valve are a combination of magnetic layers, (one pinned, one free) separated by a spacer layer, and optimized elements cannot be fabricated from simple rods or disks. However, by coupling the disk's horizontal easy axis with the rod's vertical easy axis it should be possible to create an intermediate spin state, leading to a magnetic system with three spin states (Fig. 2.3A). In systems with a pinned, high aspect ratio rod in close proximity to a free low aspect ratio disk, the free layer's magnetization is more easily switched than in the case of an isolated disk. This is due to coupling of the spins between the two segments, which pulls the free layer's magnetization out of the plane of the disk. This transient magnetization is parallel to the high aspect ratio pinned layer's easy axis and allows the disk to more easily leave its initial magnetization and relax back down to a new magnetization direction. Theory has predicted that the use of a perpendicularly aligned element creates a much more energy efficient device[20–24]. This geometry has been experimentally realized in lithographically prepared systems[21,25].

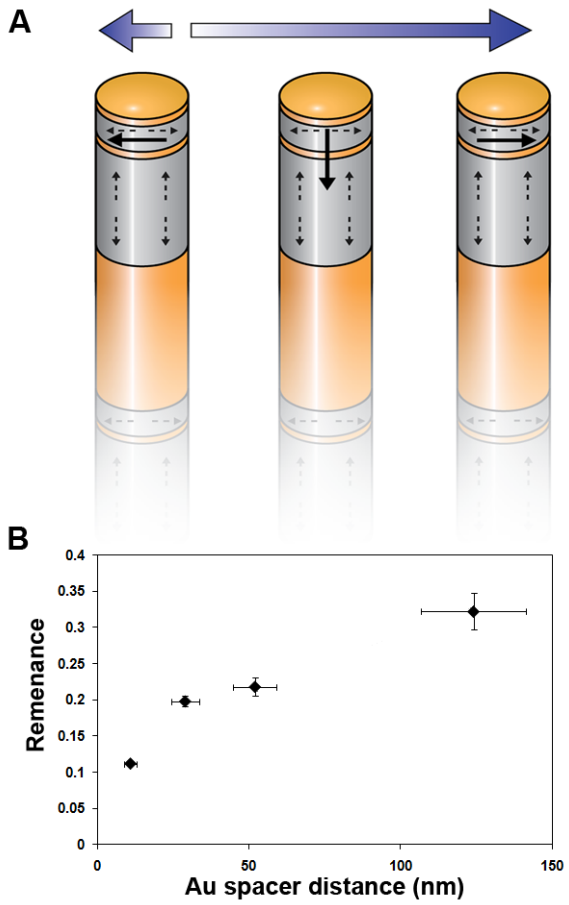

Figure 2.3. Coupling of high aspect ratio rods and low aspect ratio disks. (A). Schematic of coupling between disk and rod sections. The purple arrows indicate the magnetic field direction (perpendicular to the long axis of each nanowire), bold black arrows indicate magnetization of disks, dotted grey arrows indicate the easy axis of each magnetic segment. (B) Change in the remanant magnetization of the Ni disks with Au spacer distance. The data indicates that disk-rod coupling can be used to tune the propensity for spins to be aligned perpendicular to the plane of the disk.

We tested this further by varying the proximity of the disk element to the rod element by varying the spacer distance between the two magnetic components and probing the magnetic coupling. We begin by fabricating nanostructures in which the high and low aspect segments are placed in close proximity to one another (Fig. 2.1 C-E). When the nanostructures are placed in a magnetic field perpendicular to the longwire axis (i.e. along the plane of the low aspect ratio disks), we observe that the remanent magnetization of disks decreases with decreasing spacing between the pinned rod layer and the free disk layer (Fig. 2.3B). This data was obtained by subtracting out the signal from the rod segments using magnetization data obtained on uncoupled rods with the same dimensions. Scaling of magnetization curves between pure rod and rod-disk samples was done based on the total Ni content in the rods of each sample. The procedure allows us to more directly see the effect of coupling on the low aspect ratio segments.

The result is a three-state magnetic system where the easy axis of the high aspect ratio rod effectively creates an intermediate spin state (which has an easy magnetic axis parallel to the longwise axis) that the low aspect ratio can utilize when reversing magnetization. Since the intermediate spin state allows for lower energy switching, magnetic remanence is decreased.

2.4 Conclusion

In this work we have demonstrated how one can reproducibly and rationally design and synthesize narrow diameter (<50 nm) nanowires. Through controlled placement of magnetic and nonmagnetic sections, we have experimentally studied the coupling of various geometries of magnetic materials. We have shown that by coupling high aspect ratio magnetic rods with low aspect ratio magnetic disks we can increase the propensity of disk to switch out-of-plane by

coupling to the rod. This switching mechanism is consistent with previous work on spin systems utilizing perpendicular spin polarizers.

CHAPTER 3

Directed Self-Assembly as a Route to Ferromagnetic and Superparamagnetic Nanoparticle Arrays

3.1 Introduction

Block copolymer (BCP) systems have been gaining interest due to their ability to self-assemble into a number of morphologies.[37–39] These systems provide access to sub 10 nm size scales that may not be possible with conventional lithographic techniques.[40–49] Cylindrical phase forming polymers are of particular interest as they are able to create holes, dots, or trenches depending on their orientation to the surface, controlled by composition and molecular weight of the BCP. Additionally, nanopatterns can be produced with both orientational and positional control of the features when self-assembled block co-polymers are coupled with conventional lithography.[42,45,50–57]

In this work, we combine these block copolymer patterns with magnetic nanocrystals. As the synthesis of magnetic nanoparticles has been optimized to control size and composition[58], there have been increased efforts to find ways to organize these nanoparticles into arrays.[59–63] Magnetic nanoparticles are of particular interest for organization since the particles are able to magnetically couple when chained together.[60,61,64,65] Small area magnetic nanocrystal arrays can be made, but often these involve expensive lithographic techniques.[66,67] There have been some previous reports of organized nanoparticles using BCP; but in general these previous systems have been composed of non-interacting nanoparticles.[68–71] We note that non-noble metal

nanoparticles, in particular, are very sensitive to oxidative reactions with the substrate, even when kept in inert conditions and so to create arrays of interacting metal nanoparticles, the top layer of the pattern must be carefully controlled.

One of the most interesting magnetic nanoparticle systems is iron-platinum (FePt). The magnetic properties of FePt can be tuned not only by size but also by composition and by the nanoparticle crystal structure. FePt with a 1:1 atomic ratio is of particular interest because it can exist in two different crystal structures. Its random face centered cubic (fcc) phase is superparamagnetic. Superparamagnetism occurs in nanoscale ferromagnetic crystals when the ambient thermal energy is larger than the magneto crystalline anisotropy resulting in a material that responds to a magnetic field but shows zero net magnetization without the presence of a magnetic field. Conversely, through thermal annealing the crystal structure of the FePt can be converted to the ordered intermetallic face centered tetragonal (fct) phase.[62,72–74] The fct phase of FePt is ferromagnetic even on size scales as small as 3.5 nm diameter.[75] For these reasons FePt is expected to have possible applications in high-density data storage.[74,76,77]

Here we report experimental results demonstrating that block copolymers when combined with a directed self-assembly approach can provide high-density arrays of aligned nanopatterns with critical dimensions smaller than those of conventional lithography. We also show that these patterns can be used to organize these functional nanoparticles by controlling the precise dimensions surface of the patterns.

3.2 Results & discussion

3.2.1 Self-assembly and ALD

In this work, we make use of a poly(styrene-*b*-dimethyl siloxane) [PS-PDMS] diblock copolymer. The polymer is deposited on top of a PDMS brush polymer which is used to produce favorable interactions between the polymer and either a lithographically prepatterned or an unpatterned silicon wafer. The overall processing procedure for the films used in this study is summarized in scheme 3.1. This process can be described by 6 steps: (1) spin coat brush and anneal-strip un-grafted brush, (2) spin coat BCP onto the brush coated surface, (3) solvent anneal BCP to create a well ordered and well aligned structure, (4) two-step reactive ion etch (RIE) to selectively remove the PS block, (4) line shrinkage by ALD deposition of alumina, (6) deposition of nanoparticles. The first step in this process is crucial to create the self-assembled patterns described in this work. The use of a PDMS-OH brush is required to promote a polymer morphology composed of cylinders oriented parallel to the substrate. The grafted PDMS-OH brush also enhances wetting of the BCP film.[53] Solvent annealing has been used here in preference over thermal annealing as it enhances both orientational and long-range translational order within the PS-*b*-PDMS system.

To create a physical pattern from the block copolymer (i.e. chemical) pattern, selective etching is needed. Jung et al. have previously shown that cylinder forming PS-b-PDMS block copolymer films with parallel orientations require a CF_4 RIE etch to first remove the PDMS over-layer and a subsequent O_2 RIE step to selectively remove the PS matrix to define the PDMS pattern.[53] Figure 3.1(a) is an SEM image of a random 'fingerprint' PS-b-PDMS nanopattern after exposure to a CF_4 and O_2 plasma. The natural periodicity (L_0) of the pattern is 36 nm and the PDMS line dimension is approximately 16 nm +/-1 nm. Consequently, the spacing between the PDMS cylinders, designated L_s is 20 nm +/- 1 nm which is too large to sequester 1D chains of nanoparticles.

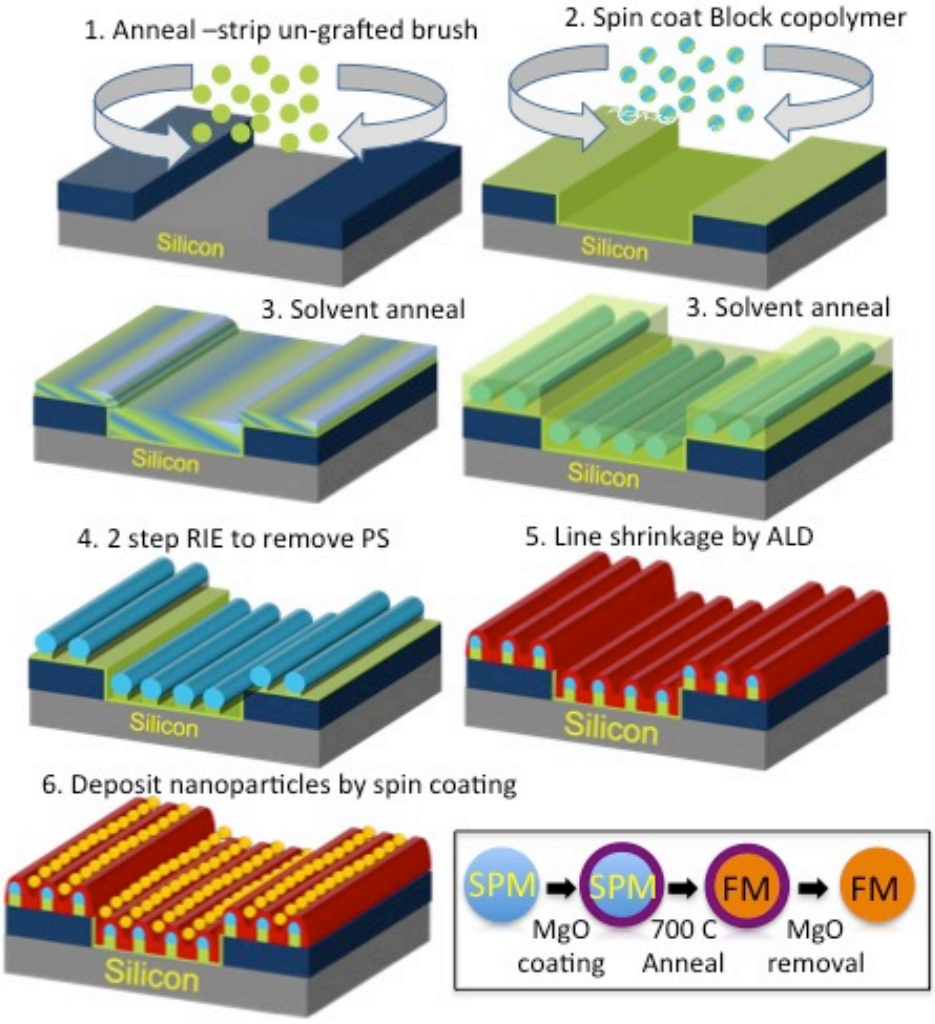

Scheme 3.1. Parts (1-6) shows a representation of the multiple step processing of aligned nanopatterns. The lower right section shows a schematic representation of the FePt nanoparticle synthesis

To reduce the gap (L_s), we deposited ALD alumina with precise thicknesses directly onto the RIE etched polymer pattern. This allowed us to reduce the gap size conformally and with nanometer precision as shown in Figure 3.1. The SEM images show a bare pattern and patterns with 5 cycles, 20 cycles, and 40 cycles of ALD respectively. The original L_s value was ~20 nm before ALD and after 40 ALD cycles (corresponding to deposition of ~4.5 nm of alumina), the L_s value was reduced to less than 10 nm. ALD deposition has been used previously to shrink the size of nanoscale feature, including nanoscale Si features created using block copolymer etch masks.[78] Selective ALD deposition has also been used to create physical matters in unetched block copolymer patterns.[79] To the best of our knowledge, however, this work is the first example of applying ALD alumina deposition directly to the etched polymer pattern to change the physical structure.

In addition to our ability to tune the trench diameter, ALD deposition has many advantages in that it can transform a very unstable nanoscale pattern into a much more robust template for further nanoscale assembly. For example, the ALD step allows us to fill in small divots caused by nanometer level over-etching, a process which ensures that our finalized patterns are consistent from batch to batch. The ALD alumina layer also acts as a solvent protection layer that lets us deposit nanoparticle onto the pattern from organic solvents that would normally dissolve or swell the block copolymers, destroying the pattern. A final advantage to the ALD process is the added thermal stability of the patterns. Figure 3.2 shows SEM images of an etched polymer pattern, that same pattern after heating to 250°C for 25 min, and a sample with 20 cycles of ALD after heating to 250°C for 25 min. Comparison between the original sample (a) and the uncoated sample (b) shows that there are large defects formed upon

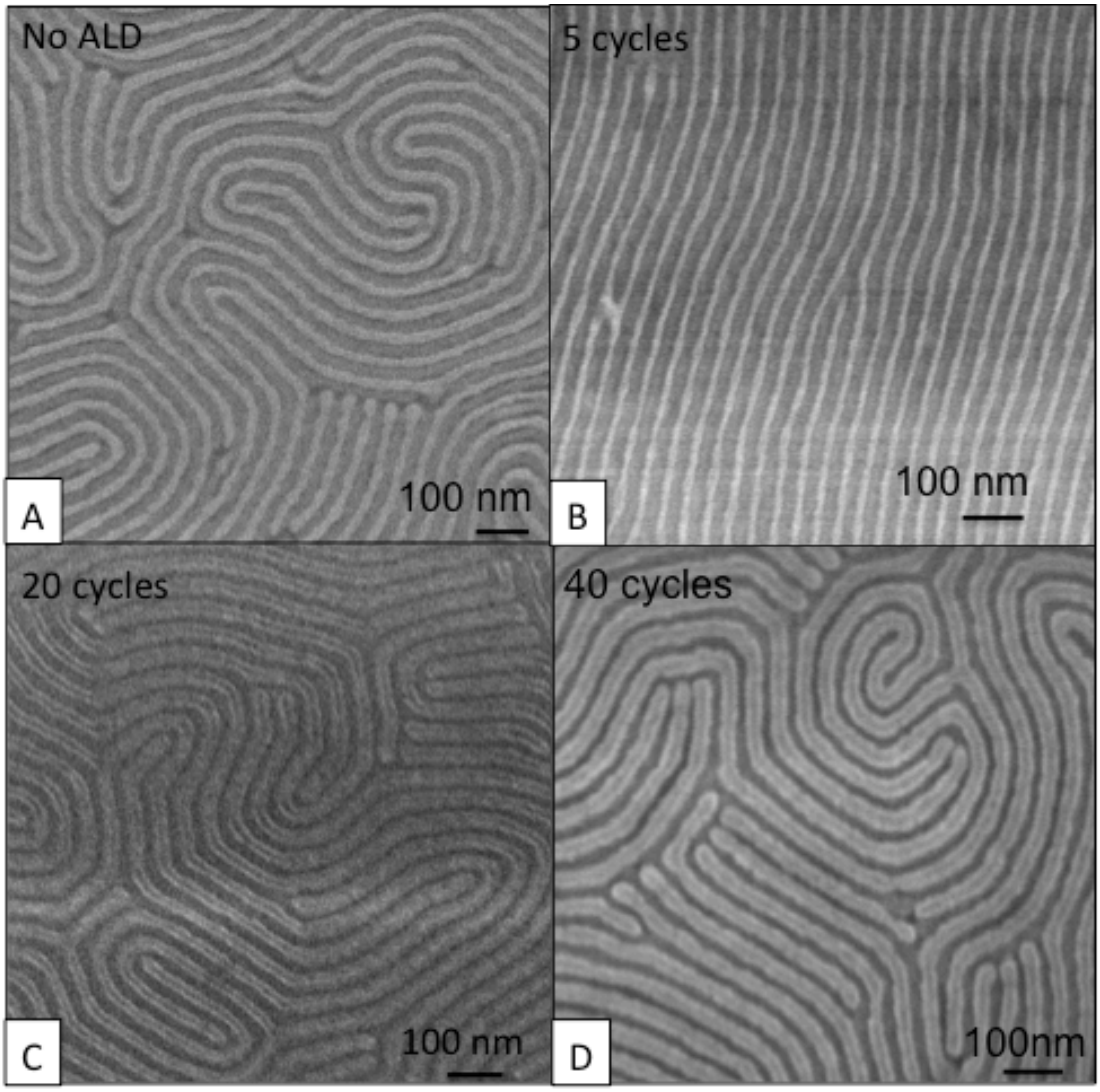

Figure 3.1. Characterization of the ALD process of random patterned BCP. Part a, shows an SEM image of a pattern prior to the ALD process. Parts b-c, shows SEM images of the patterns after 5, 20, and 40 cycles of ALD respectively. The trench spacing (Ls) is tuned controllably through this process.

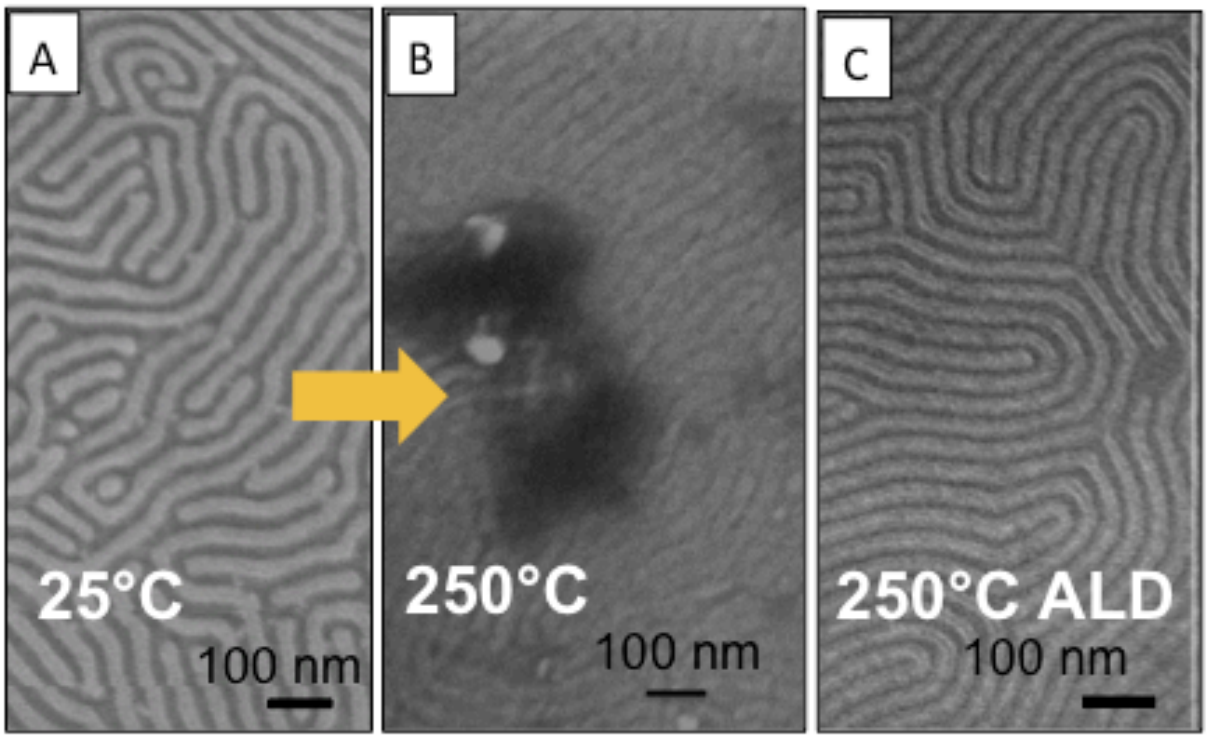

Figure 3.2. Characterization of the thermal stability of the nanopatterns. Part a shows an SEM image of the as synthesized BCP pattern. Part b shows an SEM image of the sample from part a, after heating to 250°C for 20 min. Part c shows an SEM the same sample from a, heated to 250°C after 20 cycles of ALD.

heating as well as reflow of the polymer as evidenced by reduction of the line spacing (Ls). Conversely comparison between the original sample (a) and the ALD coated sample (c) shows good retention of the morphology of the sample, other than the expected reduction in L_s due to the alumina coating.

3.2.2 Directed self-assembly

Random fingerprint patterns are excellent test structures for optimizing the ALD and NP deposition steps but in order to study dipolar coupling between nanocrystals using bulk measurements, the magnetic nanoparticle arrays must be uni-directional. Block copolymer nanopatterns can be aligned by various templating techniques, but for this work physical epitaxy was chosen as the best way to create samples that are globally aligned on the millimeter scale, which is needed for SQuID magnetometry measurements. Figure 3.3(a) shows an SEM image of a well-aligned PS-PDMS nanopattern deposited in a 300 nm trench in a Si wafer. PDMS brushes has been grafted to the silica surface of the wafer before deposition of the diblock copolymer. The patterns were annealed for 4 hr under a toluene:heptane vapor and received the same two-step RIE etch (35 second CF_4/25 second O_2) as the non-aligned samples shown above. The lithographic trench spacing was optimized to be commensurate with the BCP nanopattern to ensure defects were not created by a mismatch. One key drawback with the physical epitaxy approach is the presence of the mesa and the large fraction of the total substrate area that it occupies. One could consider removing the polymer from the mesa or reducing its size, but we chose instead to pattern both the trench and mesa regions with the same pattern to ensure that as much of the total substrate area as possible was patterned. Any un-patterned regions would

likely result in nanoparticle agglomeration. However, the level of defects does increases when self-assembly occurs on both trench and mesa regions.

Here again, an ALD step was employed to reduce L_s to a value commensurate with the average nanoparticle size (7 nm as determined by TEM, Figure 3.4(a,c)). Figure 3.3(b) shows a SEM image of an ALD coated, aligned PS-PDMS pattern confined both within a trench and on top of the mesa. The original 19 nm gap was reduced by 10 nm using a 5nm deposition ALD step. The final L_s value is 9 nm, which is ideal for sequestering a nanoparticle of about 7 nm. Unfortunately, if the reactive non-noble metal nanocrystals used here are deposited directly onto the alumina coating, they will oxidize, destroying the magnetic properties that make them interesting for this study. Therefore, a final coating step of less than 1 nm of Pt was needed to protect the FePt nanocrystals from oxidation. Figure 3.3(c) shows the patterns after a sputter coating of Pt, some roughening of the surface occurs, but this roughness does not seem to prevent deposition of the nanocrystals onto the surface.

3.2.3 FCC synthesis and FCT conversion

Two different types of nanoparticles were used in this work and the synthesis of both types of nanocrystals has been reported previously.[80,81] The lower right panel of scheme 1 describes the synthetic process used to synthesize those nanoparticles. Superparamagnetic (SPM) FePt nanocrystals were produced using a high temperature solution based decomposition of Fe and Pt precursors in the presence or organic capping ligand. SPM FePt were then converted to ferromagnetic (FM) FePt by individually coating the nanoparticles with MgO and then dry heating the MgO/FePt powder to drive the fcc to fct phase transition. Figure 3.4(a) shows a TEM image of the as synthesized SPM FePt and a TEM of the MgO coated SPM

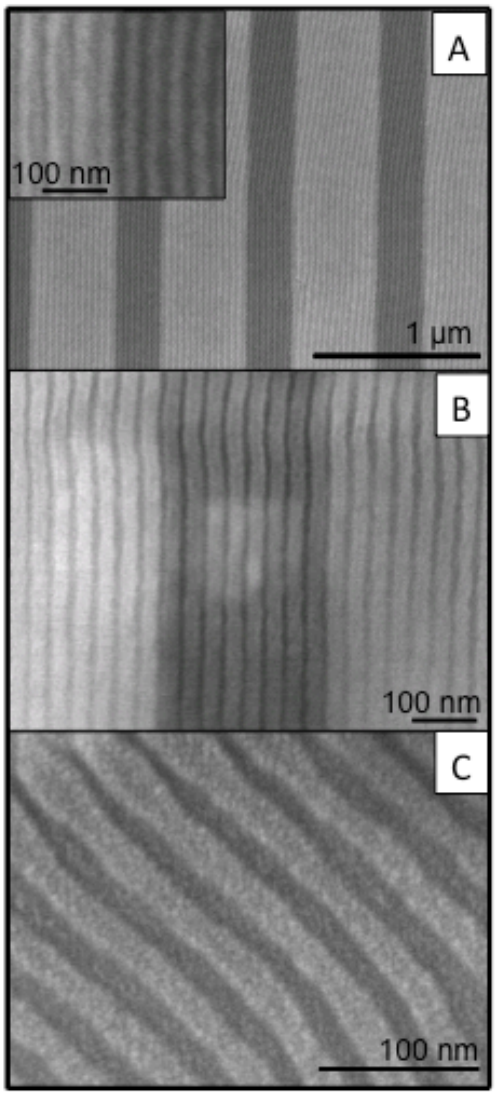

Figure 3.3. shows SEM images of the aligned substates. Part a shows the aligned substrate after RIE. Part b shows the nanopattern after 40 cycles of ALD, resulting in a trench size of ~ 10 nm. Part c shows the nanopattern after ~0.5 nm of Pt sputtered to the surface to create a non-oxide surface for the nanocrystals.

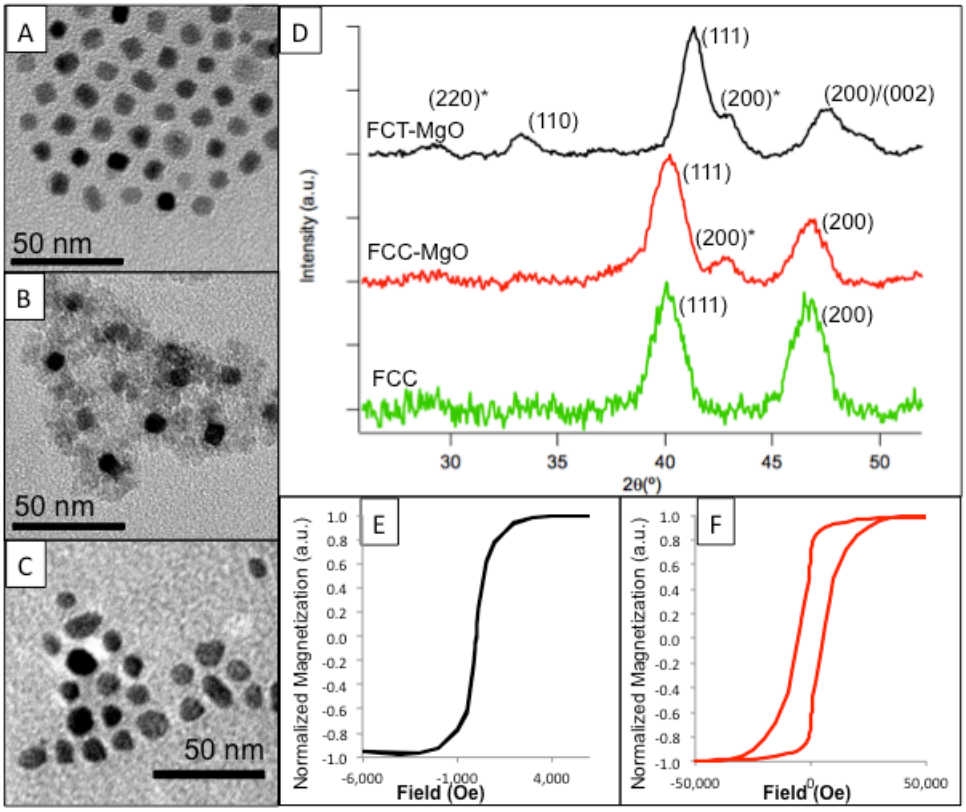

Figure 3.4. Characterization of FePt nanocrystals. Part a-c, shows a TEM image of the as synthesized SPM nanocrystals, SPM nanocrystals coated in MgO, and FM nanocrystals removed from the MgO as described in scheme 1. Part d shows powder XRD diffraction data on the samples described in part a-c. Part e and d shows magnetic hysteresis curves of the SPM and FM magnetic nanocrystals at 298 K.

nanocrystals is shown in figure 3.4(b). Finally, the MgO was removed in solution and replaced with organic capping ligands (figure 3.4(c)). Soluble, ligand capped versions of both the SPM and FM nanoparticles were then directly deposited on to the BCP patterns under inert conditions. Details about these processes can be found in the experimental section.

As discussed previously the SPM phase is present in the face centered cubic (fcc) structure of the material and after thermal annealing to the FM phase the structure converts to the face centered tetragonal (fct) structure. This conversion can then be confirmed by x-ray diffraction as shown in figure 3.4(d). After coating with MgO the fcc structure is retained and there is an additional peak that corresponds to the MgO (200). After thermal conversion the FePt (200) peak splits to the (200)/(002) peaks, additionally the fct (110) can also be seen confirming the conversion from the fcc to the fct structure.

Sample magnetization as a function of applied magnetic field (i.e. magnetic hysteresis loops) was measured at room temperature for both the SPM and FM nanocrystals, as shown in figure 3.4(e,f) respectively. The magnetic measurements confirm that the as synthesized fcc nanoparticles are superparamagnetic. After thermal annealing the coercivity of the fct nanocrystals increases to 10,000 Oe and the ratio of the remanant magnetization to the saturation magnetzation is 0.75, as is expected in a ferromagnetic material. The FM nanoparticles used were made from the same batch of SPM nanoparticles used in this study. This allowed consistency between the stoichiometry of the samples as well as the overall nanoparticle size and polydispersity. FM nanocrystals with larger coercive fields can be created with longer annealing times, but those nanocrystals quickly aggregate in solution and cannot be processing in BCP trenches. As seen in figure 3.6b below, the least aggregated and thus most processable

nanocrystals in solution tend to have significantly smaller coercive fields than the sample average.

3.2.4 Directed deposition/placement of NPs within BCP patterns

Nanoparticle deposition was achieved by spin-coating semi-dilute (approx. 0.1 - 1 mg/ml) solutions of nanoparticles from chloroform at high spin speeds (i.e. 9000 rpm) onto aligned PS-*b*-PDMS patterns. Figure 3.5(a,b) shows an SEM images of the SPM and FM nanocrystals deposited onto the aligned substrates as described above. The deposition of the nanocrystals gives almost full coverage of the substrates with one-dimensional nanocrystal chains. As shown in the inset of Figure 3.5(a), however, there are many breaks where the chains are not complete, so this system does not contain infinite 1-dimensional coupling. The inset also shows that there are a few regions where the trenches are wider and nanoparticles stack 2 and 3 particles across.

Despite the defects shown in the Figure 3.5a inset, the images in figure 3.5a and b make it clear that the majority of the population contains 1D nanocrystal chains. This is one of the benefits of the processing steps described previously – the ability to tune the number of nanocrystals in each trench and specifically to create trenches that trap 1D chains of nanocrystals, if fewer ALD cycles were used, one should be able to create zig-zag and dimer chains of particles, as shown previously using trenches of different diameters.[63]

3.2.5 Magnetometry analysis of coupled nanoparticles

Magnetic measurements were performed on the samples shown in figure 3.5, with the exception that the samples were capped with 25 nm of Au to prevent oxidation. To study the coupling between magnetic nanocrystals in chains, magnetization was measured with the unique

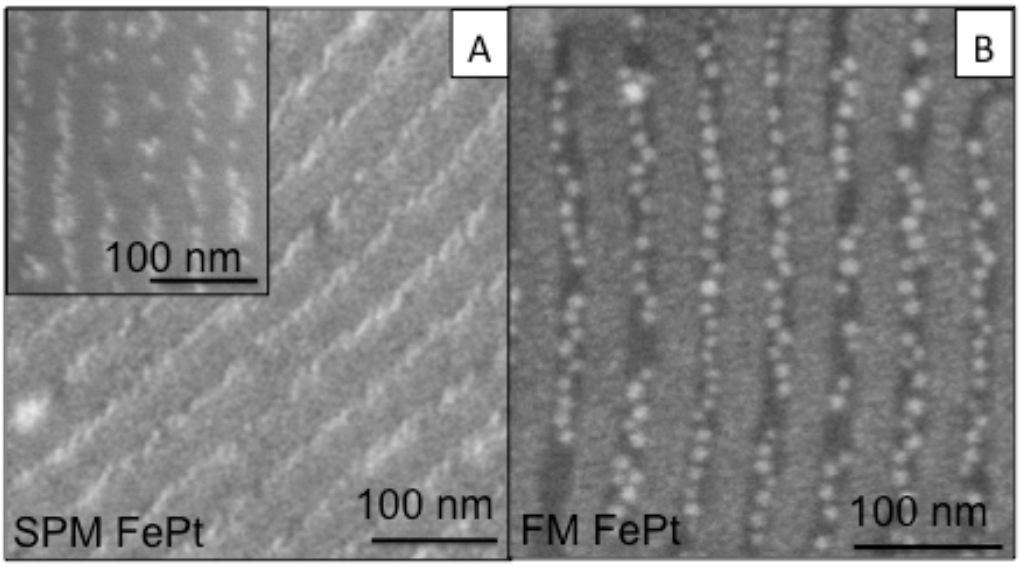

Figure 3.5. Characterization of nanoparticles in aligned substrates. Part a shows arrangement of SPM FePt nanocrystals and part b shows FM FePe nanocrystals organized into mostly 1D chains.

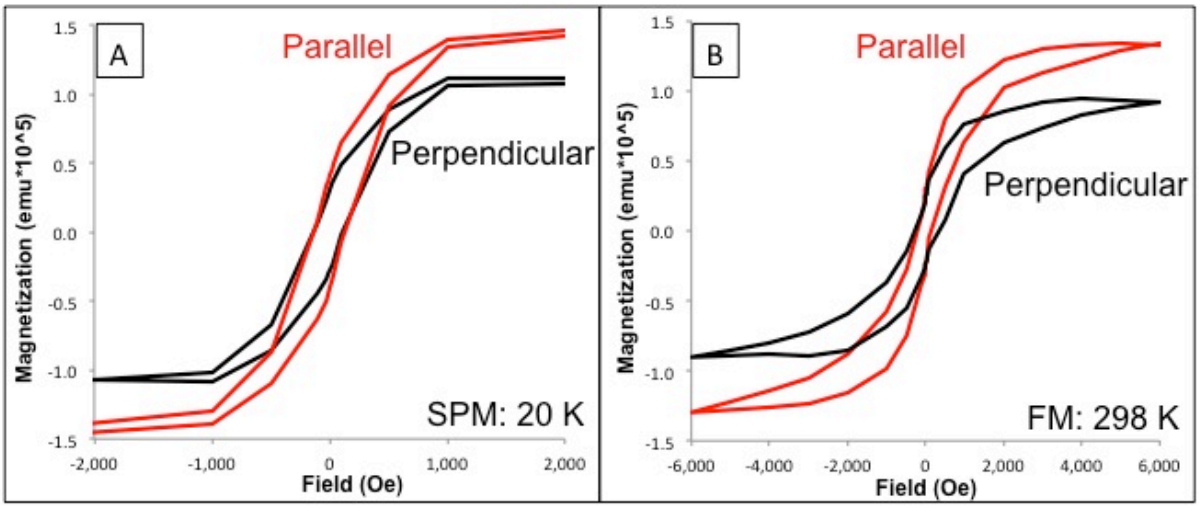

Figure 3.6. Magnetic hysteresis curves obtained on aligned substrates. Part a shows SPM nanocrystals measured at 20 K. Part b shows FM nanocrystals measured at 298 K. Samples are measured with the magnetic field applied along the trenches (parallel, red), and orthogonal to the trenches (perpendicular, black).

axis of BCP patterns oriented both parallel and perpendicular to the applied magnetic field. Figure 3.6(a) shows magnetic moment (M) measurements as a function of applied magnetic field at 20 K for the fcc/SPM sample. This temperature is below the SPM-to-FM transitions for these nanocrystals; we chose this temperature so that we could measure coupling between magnetic dipoles for chains nanoparticles produced by the BCP pattern. This coupling is expected to be washed out by thermal fluctuations at room temperature. The fcc/SPM particles have a coercivity of 200 Oe at 20 K, confirming their ferromagnetic nature.. When the samples are measured with the applied field parallel to the trenche axis, the magnetic saturation is increased by 33%, compared to measurements made perpendicular to the chains. This enhancement in magnetization arises from the creation of a magnetic easy axis along the trench direction. The symmetry breaking that causes this new easy axis confirms magnetic coupling along the nanocrystal chains.

Similarly, figure 3.6(b) shows room temperature magnetization measurements made at on the FM sample. The samples show a coercivity of 800 Oe, confirming that these samples are ferromagnetic. Similar to the SPM particles, the samples show an enhancement of the saturation magnetization of 35% when measured with the applied field parallel to the channels compared to the saturation magnetization measure with the applied field perpendicular to the channel direction. This anisotropy again indicates the creation of a magnetic easy axis along the channel direction due to coupling between magnetic nanocrystals.

All samples clearly show magnetic anisotropy that correlates with the structural anisotropy seen in figure 3.5. The difference in the saturation magnetization measured parallel to the channel axis is less than a factor of 2x greater than that measured perpendicular to the channel axis, however. The modest increase in saturation magnetization is expected for the

fcc/SPM samples measured at 20K, as these samples are not terribly far below their blocking temperature (~50K). The modest increase is somewhat more surprising for the FM sample, as bulk versions of these nanocrystals show a coercive field of 1 tesla (T) at room temperature, implying a stable hard magnetic axis that should produce strong dipole-diploe coupling along trenches. The coercivity for nanocrystals in trenches is nearly 10x smaller than this 1T value, however, and this likey occurs because the least magnetic nanocrystals are the ones that are least clumped in solution, as discussed above. Large agglomerates of nanocrystals are likely to be spun off during nanoparticle deposition, but isolated nanocrystals can be efficiently trapped in trenches. Indeed, we specifically heated these samples for only 3 hours, rather than the standard 7 hours needed for complete conversion to the fct phase in an effort to reduce clumping of nanocrystals during the deposition on the substrates.[80,81] From the difference in coercivities observed in figures 3.4 and 3.6, however, significant aggregation in solution still occurred, and the nanocrystals that were deposited into the trenches were the least magnetic part of the sample. This should reduce the dipole-dipole coupling between nanocrystals in trenches. In addition, we do not know if the unique tetragonal axis of the nanocrystals can align along the channel direction during the deposition process, or if there is competition between randomly oriented nanocrystal easy axes and a global easy axis created by coupling between nanocrystals. While we cannot fully explain the magnitude of the magnetic anisotropy in these samples, all films show distinct magnetic anisotropy, indicating coupling between magnetic nanocrystals in chains.

3.3 Conclusions

Self-assembled trench arrays were made using diblock copolymers with one easily etchable block. Random “fingerprint” patterns were made on flat substrates and straight aligned

patterns were produced by deposition into lithographically generated tranches. We have further shown that we can tune the trench size (L_s) by precise ALD alumina desposition. The ALD process is beneficial as it makes the patterns more thermally robust and it protects the patterns from solvents that could be needed in later processing steps. This process results in a global alignment of trenches with tunable size and surface composition.

These substrates create an ideal platform to study the coupling of magnetic nanoparticle arrays. Here we used both superparamagnetic and ferromagnetic FePt nanocrystals. We showed that linear arrays of nanocrystals could be produced using trenches that were size matched to the nanocrystals. The nanocrystal arrays showed magnetic coupling along the chains of nanocrystals suggesting that this process can be used to create interacting magnetic nanoparticle arrays. Similar arrays may find interesting applications in future magnetic devices that rely on unidirectional coupling between nanocrystals.

3.4 Experimental

3.4.1 Materials: For the FePt synthesis iron pentacarbonyl (98%, Aldrich), oleic acid (90%, Aldrich), oleylamine (>70%, Aldrich), 1-octadecene (90%, Aldrich), 1,2-tetradecanediol (98%, Aldrich), $Pt(acac)_2$ (98%, Strem), $Mg(acac)_2$ (98%, Strem), and hexadecanethiol (90%, Alfa Aesar) were used as received without further purification.

All hydroxyl-terminated homopolymer and the diblock copolymer were supplied from Polymer Source, Inc. and used as received. The brush layer was hydroxy-terminated polydimethylsiloxane with a molecular weight of 5.3 kg mol^{-1}. The diblock copolymer was a lamellar-forming symmetric poly(styrene)-block-poly(methyl methacrylate) (PS-*b*-PDMS) with an M_w of 42.0 kg mol^{-1} (PDI $\leq$ 1.1).

3.4.2 FCC/FCT Synthesis: *Synthesis of ~7 nm SPM – FePt nanocrystals*: A solution containing 0.5 mmol of $Pt(acac)_2$, 10 mL of 1-ocatadecene, 4 mmol of oleic acid, and 4 mmol of oleylamine was stirred in a 250 mL 3 neck flask under a gentle argon flow. The solution was heated to 120°C at a rate of 6°C/min. This temperature was held for 13 min to insure full dissolution of the Pt precursor. At this point 0.20 mL of iron pentacarbonyl was added. The solution was then heated to 240°C at a ramp rate of 3°C/min and refluxed at this temperature for 1 hour. The solution was then cooled and the particles were precipitated with ethanol and centrifuged. Two further washings were done with ethanol and hexane followed by centrifugation. The particles were then dispersed in 10 mL of hexane.

Synthesis of MgO coated SPM-FePt nanocrystals: A solution of 2 mmol of $Mg(acac)_2$, 4 mmol of tetradecanediol, 4 mmol of oleic acid, 4 mmol of oleyamine, and 20 mL of benzyl ether was stirred in a 250 mL 3 neck flask under gentle argon flow. The solution was first heated to 80°C and held at this temperature to insure dissolution of the precursors. Next 5 mL of the FePt particle solution obtained above was injected into the flask rapidly. The solution was then heated to 120°C and held for 20 min to insure all of the hexane was removed. Finally the solution is then quickly heated to 298°C and refluxed at this temperature for 1 hr. The particles were collected and purified via the same procedure described above.

3.4.3 Self-assembly of the PS-*b*-PDMS nanopatterns: All silicon substrates were cleaned in fresh piranha solution (3:1) at 85°C for 1 hr. The PDMS-OH brush was deposited from a 1.5% weight solution onto silicon and grafted to the native oxide by annealing at 150 °C for 16 hr under vacuum. The un-grafted polymer brush layers were removed by sonication in toluene.

The 34.0-11.0 kg mol^{-1} (42.0 kg mol^{-1}) cylinder-forming PS-*b*-PDMS has a natural periodicity (L_0) of 36 nm. BCP films with a final thickness of ~40-45 nm were cast from 0.5% weight solutions in carbon-tetra-chloride by spin coating at 6000 rpm for 20 seconds. The block copolymer patterns were solvent annealed with toluene:heptane (3.5:1) solution for 4 hr periods. The nanopatterns were developed using a 2 step reactive-ion etching (RIE) process on STS AOE to first remove the PDMS over-layer (CF_4, 100W) and next to selectively remove the PS matrix (O_2, 100W).

3.4.4 Directed self-assembly of the PS-*b*-PDMS nanopatterns: Patterned oxide substrates were used for graphoepitaxy alignment of the PS-PDMS patterns. The final trench dimensions were ~300-400 nm wide, 35-45 nm deep with a pitch of 900 nm. The final patterned regions were 6 mm x 6 mm to ensure that the DSA was global and also to provide ideal sampling for SQuID measurements. The PS-*b*-PDMS patterns were deposited, solvent annealed and etched on the patterned wafers using the same parameters outlined in the previous sections.

3.4.5 ALD Al_2O_3 nano-gap reduction and Pt-Sputtering: Atomic layer deposition (ALD) of amorphous alumina (Al_2O_3) was performed in a Savannah 100 (Cambridge NanoTech Inc.) operating at 250°C at 20 mTorr. Trimethylaluminum and H_2O were used as the sources of aluminum and oxygen, respectively, and a 20 sccm continuous nitrogen flow rate was used throughout the deposition. The deposition rate of Al_2O_3 was 0.11 nm per cycle (i.e. 10 cycles = 1.1 nm). Depending on the PDMS cylinder-to-cylinder spacing, the conformal coating was tuned to be commensurate with the nanoparticle size. Pt sputtering was done using a Hummer 6.2 from Anatech.

3.4.6 NP release and deposition: The MgO coated SPM-FePt, nanocrystals were heated in a tube oven at 750°C under a flow of 5% hydrogen gas and 95% argon gas for 3 hours to convert them to the FM crystal structure. The collected powder was then washed with a dilute HCl solution (10% vol) and a chloroform solution containing hexadecanethiol and oleic acid. The vial was sonicated for ~ 10 mins and then shaken for 30 min. The dispersed FM-FePt particles were collected from the chloroform layer and spun onto the patterned substrates from this solution.

SPM and FM nanoparticles were deposited *via* spin-coating methods in an argon atmosphere to minimize oxidation of the nanoparticle arrays. SPM/FM nanoparticles were deposited at 8000 rpm from chloroform solutions onto the ALD-coated, etched PS-*b*-PDMS nanopatterns. Samples were protected from oxidation for magnetometry measurements by depositing a thin Au coating (~25 nm) *via* thermal evaporation and sealing in kapton in an argon atmosphere.

3.4.7 Characterization: Wide angle x-ray scattering (WAXS) measurements were carried out on a Bruker D8-GADDS diffractometer (Cu Kα radiation). Scanning electron microscopy (SEM) was performed on a JEOL JSF6700 with a semi in-lens detector operating at accelerating voltages of 3 kV. All samples were imaged without any additional metallic coatings. Low-resolution transmission electron microscopy (TEM) was performed using a FEI CM120 system operating at 120 kV. A Quantum Design MPMS super-conducting quantum interference device (SQuID) magnetometer was used to measure hysteresis loops and remanence curves at various temperatures.

CHAPTER 4

Mesoporous Bismuth Ferrite with Electric Field Amplified Ferromagnetism

4.1 Introduction

Magnetoelectric materials have been the focus of much research due to their possible application in spintronic and memory based devices [82,83]. These are a type of material, which combines ferromagnetism and ferroelectricity in a single material allowing control of one parameter through the other [8]. Ferroelectricity is when a material poses a spontaneous electric dipole; similarly ferromagnetism is when a material poses a permanent magnetic dipole. Few materials achieve this intrinsically where both of these properties are present in a single material; even fewer achieve this at room temperature. There does exist a material, bismuth ferrite $BiFeO_3$ (BFO), that is magnetoelectric, also known as multiferroic, at room temperature and for this reason it is one of the most widely researched examples of a multiferroic material [10,12]. Additionally a class of materials known of hexaferrites, due to their hexagonal crystal structure, has been shown to have a few examples of room temperature multiferroics [13]. One such example is $Sr_3Co_2Fe_{24}O_{41}$ [14]. Though there are a few different room temperature multiferroic systems that could be studied as discussed above this study will focus on BFO, but the methods presented here could possibly be extended to other systems such as the hexaferrites.

Recently, experiments utilizing strain-layer epitaxy have shown that magnetic and ferroelectric polarizations can be amplified by introducing lattice strains into these materials [11,12,84–86]; strain has also been used to convert materials that are neither ferroelectric nor ferromagnetic to ferroelectric ferromagnets at low temperatures [87] as well; however, the strain

introduced in these systems is often isotropic. Studies have shown that non-isotropic strain states can have huge effects on the induced magnetization of the material [88]. Here we seek to exploit this finding, using nanoscale architecture to create non-isotropic strained structures in a room temperature single-phase multiferroic without the need for epitaxy.

In the bulk, BFO belongs to the R3c space group, with a rhombohedral distortion of the perovskite structure along the pseudocubic $[111]_{PC}$ [89]. BFO shows ferroelectric polarization, with a Curie temperature of ~1,100 K, and antiferromagnetism via 'G-type' ordering of the Fe^{3+} ions with a Neel temperature of ~640 K [90]. However, neighboring spin interactions between Fe^{3+} centers produce an antiferrodistortive tilting of the iron octahedra resulting in <2° spin canting and weak ferromagnetism [10,12]. BFO thin films engineered with epitaxial strain have reported saturation magnetization (M_S) values of 0.5 Bohr magnetons (μ_b/Fe) and polarizations of up to 60 microcoulombs per square centimeter ($\mu C/cm^2$), [86,91] which are substantial improvements relative to bulk magnetization and polarization values of 0.05 μ_b/Fe and 10 $\mu C/cm^2$, respectively [86,92]. Theoretical studies have suggested that BFO's polarization is susceptible to strain [93,94]. More recently He et al. have reported a large increase in the spontaneous magnetization of a highly anisotropically strained mixed phase (rhombohedral, super-tetragonal), compared to bulk pure rhombohedral phase BFO, 0.2-0.3 (μ_b/Fe) [88]. This mixed phase system was able to create highly magnetic local domains. Here we present an alternative approach for producing thin film BFO with anisotropic strain states using templated porous nanostructures that show high magnetization that can be induced upon application of electric field.

Evaporation-induced-self-assembly (EISA) techniques using an ampiphilic diblock co-polymer and inorganic precursors can be used to produce thin films of crystalline phases with nanoporous architectures [95] [see SI for details of this synthesis]. Previous thin film studies of

mesoporous frameworks composed of magnetostrictive cobalt ferrite ($CoFe_2O_4$, CFO) revealed that flexing and contracting of the pores upon high temperature crystallization produced highly anisotropic strain states parallel and perpendicular to the plane of the substrate. This structural anisotropy resulted in magnetic anisotropy in the frameworks [5]. In this report, we demonstrate that the strain states achieved from EISA based, epitaxial-free mesoporous templating results in polycrystalline BFO films exhibiting magnetoelectric coupling that exceed those reported previously for their dense thin film counterparts.

4.2 Results and Discussion

Scanning electron microscopy (SEM) studies of porous but amorphous BFO frameworks indicate that the materials have homogeneous porosity throughout the film (figure 4.1B). 2-dimensional small angle X-ray scattering (2D SAXS) further indicate the amorphous films have scattering maxima consistent with a somewhat disordered a cubic network of pores. Both in and out-of-plane q-spacings are consistent with previously reported studies employing related polymer templates (figure 4.1A)[5]. The elliptical nature of the diffraction pattern indicates that the pores have shape anisotropy, with a significant out-of-plane compression [5]. This anisotropy in the framework results because the films are anchored to the silicon substrate, eliminating movement in-plane. Stress relaxation thus proceeds by out-of-plane compression of the pores only. Upon further thermal annealing to achieve crystallization of the framework, some restructuring of the mesoporous structure is observed (figure 4.1D), but the porosity remains homogeneous. This partial disordering results in a loss of out-of-plane scattering in 2D SAXS measurements because of the finite film thickness, but in-plane scattering is still (figure 4.1C). For templated films that exhibited poor long-range periodicity in their amorphous state (not

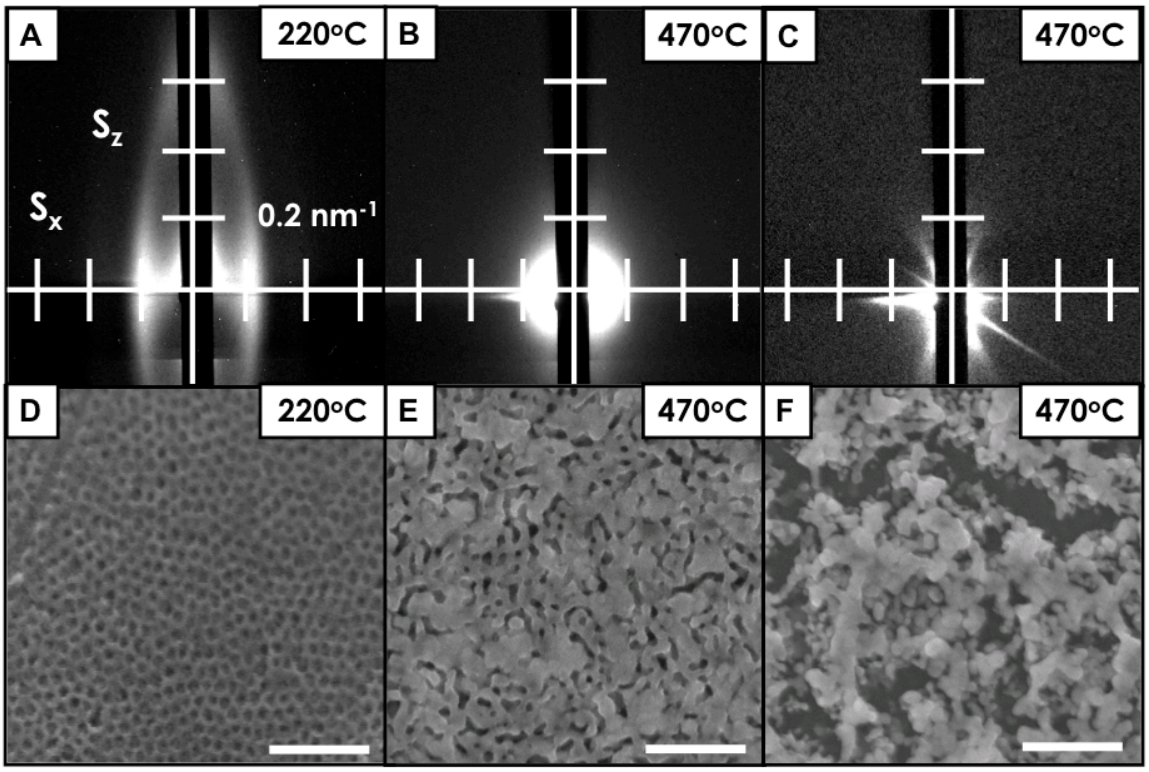

Figure. 4.1 SEM and synchrotron-based 2D-SAXS measurements of BFO mesoporous films displaying frameworks that are amorphous (A, D), crystallized with retention in-plane ordered porosity (B, E) and crystallized with complete loss of ordered porosity (C, F). SAXS patterns were collected at an angle of incidence $\beta=0.1^{o}$.

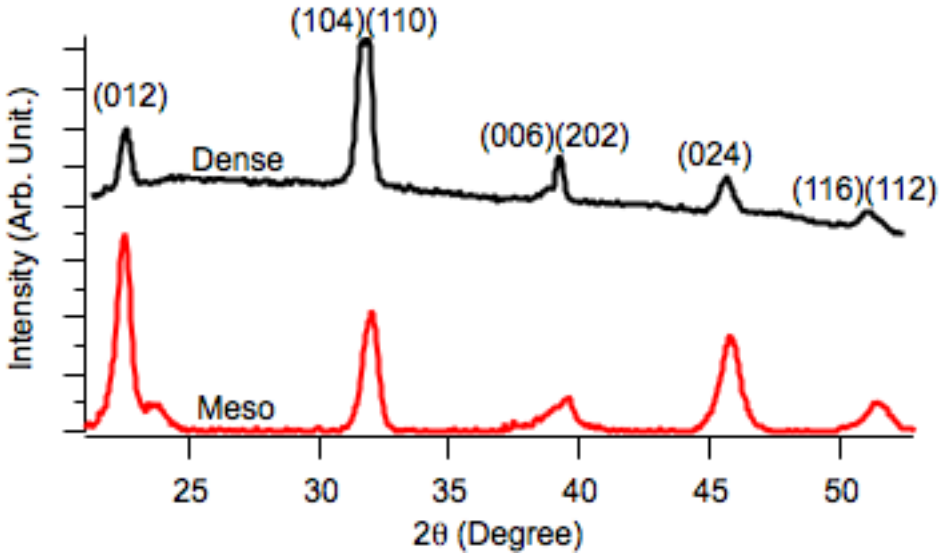

Figure. 4.2 Powder XRD obtained on mesoporous (top curve, red), and dense (bottom curve, black) BFO thin films. Peaks correspond phase pure BFO (JCPDS #01-071-2494).

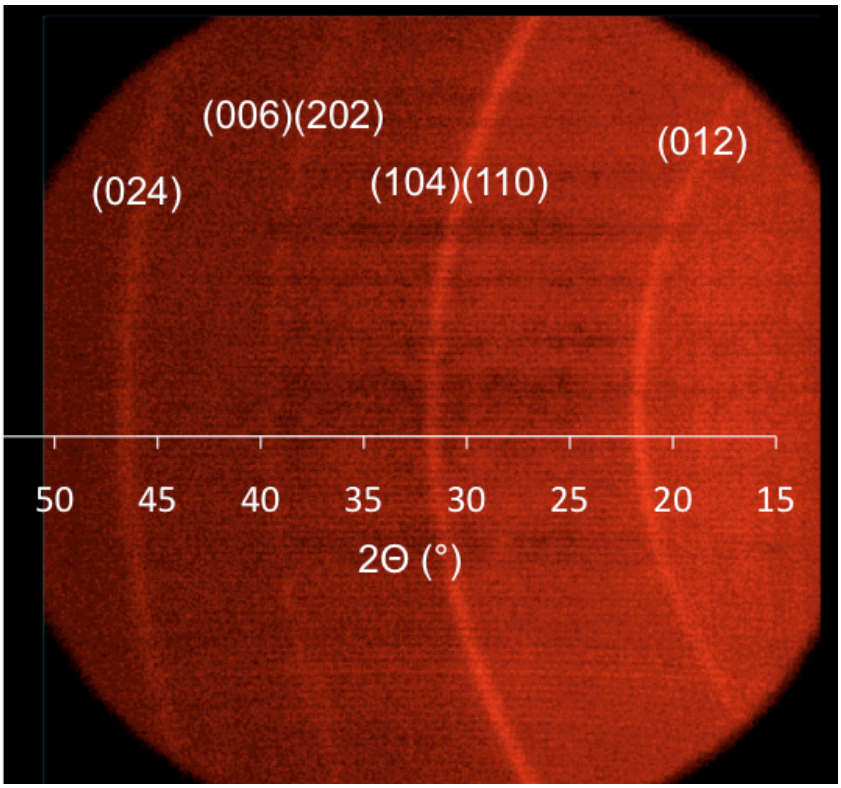

Figure. 4.3 2D-XRD on the polycrystalline films shows smooth rings in the 2D diffraction suggesting no preferred orientation of the films (JCPDS #01-071-2494). Data was taken on a D8-GAADS diffractometer.

shown) or films that were heated too long, after crystallization films were cracked and a release of in-plane stress was observed through the formation of islands (figure 4.1E,F). For all BFO films, both porous and non-templated dense materials, phase pure materials were achieved, as confirmed by x-ray diffraction (XRD) measurements (Fig. 4.2). The polycrystalline films possess no preferred domain orientation, as determined by 2D-XRD (JCPDS 01-071-2494)(Fig. 4.3).

Piezoelectric Force Microscopy (PFM) measurements allow for the visualization of ferroelectric properties through application of an electric field, employing the PFM tip as the top electrode and a conducting substrate as the bottom electrode. Concentric boxes of alternating polarization direction were written into the BFO framework illustrating the presence of a switchable ferroelectric dipole moment that is stable at room temperature (figure 4.4A). The piezo-force curve in figure 4.4B shows that application of a modest field can be used to switch the ferroelectric domain. Magnetic properties of the mesoporous and dense BFO films were investigated via SQuID magnetometry. Magnetization curves (M vs H) for both mesoporous and dense BFO films revealed all systems to be ferromagnetic at room temperature, as noted by small but measurable coercive widths and magnetic saturation values (M_S) of 0.04 and 0.001 m_b/Fe, respectively (Fig. 4.5).

The magneto-electric coupling for the mesoporous BFO films can determined by applying modest electric fields to the films (poling) followed by evaluating the change in magnetic properties *ex-situ* in a SQuID magnetometer. The magneto-coupling is then determined from the change in magnetization at low applied magnetic fields as a function of applied electric field. At zero poling fields the magnetic susceptibility, (dM/dH), measured perpendicular to the poling direction in the ordered mesoporous BFO was 5.8×10^{-5} μ_b/(Fe*Oe), upon poling this

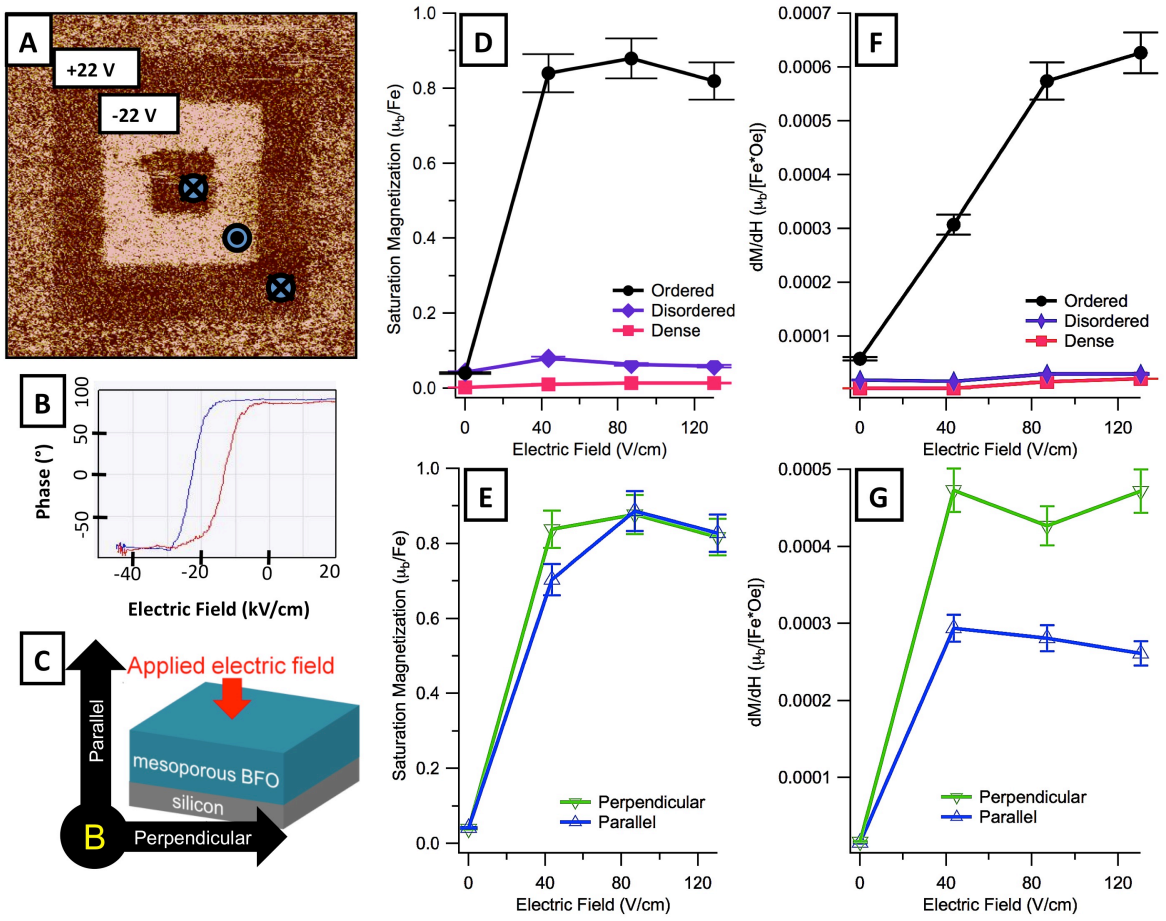

Figure. 4.4 Magnetoelectic characterization of mesoporous and dense BFO films. (A) PFM phase image showing response to positive and negative fields for mesoporous BFO sample. (B) Phase vs electric field curve of BFO sample from (A). (C) Schematic of the relative electrical poling and magnetic field orientations used in magneto-electric coupling experiment. Modest external electric fields are used to control the magnetization of BFO films. Films prepared with ordered mesoporous architectures show superior magneto-electric responses versus dense and disordered porous films, as greater changes in total saturation magnetizations (D), and magnetic permeability (F), were observed. SQuID measurements displaying the effects of electric field on the saturation magnetization (E) and permeability (G), for a mesoporous films oriented parallel and perpendicular to the external magnetic field.

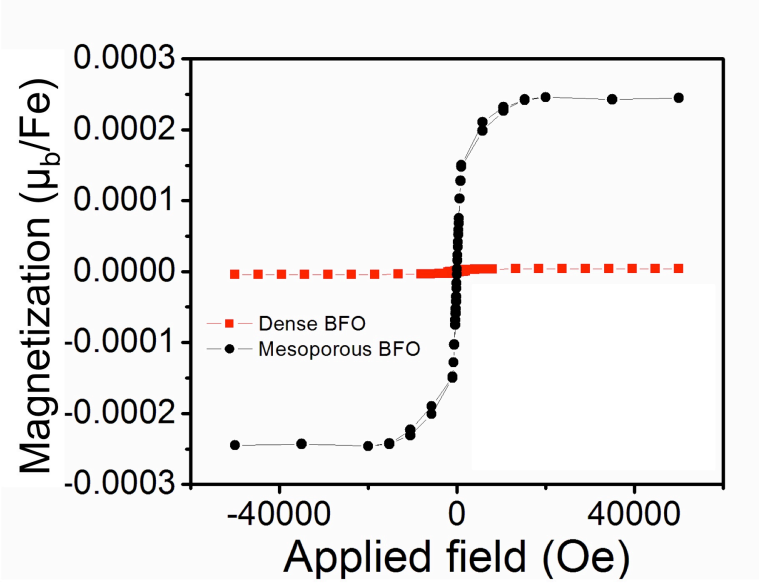

Figure. 4.5 Magnetization versus Field hysteresis curves for dense and mesoporous films prior to electrical poling. This results shows even before application of an electric field the as prepared Mesoporous BFO has a much higher saturation magnetization than its dense counterpart.

increased 10-fold to 6.3 x10^{-4} μ_b/(Fe*Oe) (Figure 4.4F). With the same applied field, the change in the dense sample is minimal. Anisotropy in the magnetoelectric coupling was also observed for porous films measured with magnetic field applied either perpendicular and parallel to the electric field poling direction (figure 4.4G). In agreement with theoretical predictions, higher coupling is observed when there is a perpendicular relationship between the two fields because the electric poling establishes an orthogonal magnetic easy axis [84,96]. The large increase in magnetic susceptibility values in both directions is contrary to theoretical predictions on unstrained systems, however [84].

The apparent contradiction can be resolved by the observation that a large part of the change in the dM/dH values upon electrical poling arises not from establishment of a magnetic easy axis, but instead from an increase in the saturation magnetization (M_s) upon electric poling. Figure 4.4D,E shows the surprising result that application of modest external electric fields dramatically increased the M_S values of the ordered mesoporous films. Figure 4.4D indicates that ordered mesoporous BFO shows an increase from 0.04 to 0.82 m_b/Fe upon application of a modest electric field. The non-templated sol-gel BFO, which is mostly dense, shows a much smaller increases in M_S, changing from 0.001 to just 0.014 m_b/Fe upon application of the same field. The change in M_S is equivalent measured either parallel or perpendicular to the applied field (figure 4.4E), a result that suggests the change arises from an intrinsic bonding change in the material, rather than the formation of a magnetic easy axis. We also note that the low M_s values in the unpoled samples preclude iron oxide impurities from the sol-gel synthesis as the source of the high magnetization in poled samples. These M_s values for electrically poled mesoporous BFO films demonstrate the highest recorded for BFO films to-date. Previously,

epitaxially strained BFO thin films reported M_s values of 0.5 m_b/Fe [91] and doubly strained BFO domains showed local values of 0.2-0.3 m_b/Fe [88].

It is important to consider the role played by the nanoscale architecture in controlling this large increase in saturation magnetization upon electric poling. When samples are crystallized with a loss of homogeneous nanoscale porosity and strain release due to cracking (figure 4.1E,F), samples show little change upon electrical poling. Figure 4.4D indicates that there is an increase in M_s from 0.04 to 0.06 m_b/Fe upon electric poling in these aperiodic samples. Strain induced by nanoscale periodicity appears to be key to the magnetoelectric coupling observed here.

To probe the origin of the amplified magneto-electric coupling for ordered mesoporous BFO films versus their dense counterparts, synchrotron based grazing incidence, high-resolution, wide-angle diffraction studies were conducted. As mentioned, the bulk space group is R3c. However, for simplicity, planes are indexed in R3m, which is based on the cubic lattice, allowing for easier visualization of the lattice changes. The (100), (110) & (1-10) lattices planes were investigated as a function of applied electric field to observe changes in the lattice. The latter pair of reflections provides a measure of the rhombohedral distortion from the cubic lattice. The cubic (110) splits from a single peak into the rhombohedral (110) (1-10) pair (JCPDS 01-071-2494). Since the samples are comprised of randomly oriented polycrystalline domains, all peaks could be observed in both in-plane and out-of-plane orientations, allowing us to use these peaks as a probe of the strain state of the porous BFO.

The application of an external electric field induced changes in the lattice spacings of mesoporous BFO while dense BFO lattices planes were essentially unaffected by electrical poling. For mesoporous BFO, lattice planes both perpendicular and parallel to the poling direction displayed an overall contraction upon electrical poling (figure 4.6A, C), compared to

the dense BFO, which shows essentially no change (figure 4.6B, D). This contraction is summarized in Table 4.1 showing at least an order of magnitude larger slope for mesoporous samples compared to dense in all planes; (100), (1-10), (110). The fact that the mesoporous lattice spacings can change to in response to electrical poling may stem from increased flexibility of the porous framework. In addition to the contraction, a reduction in splitting between the out-of-plane (110) and (1-10) lattice planes was observed (figure 4.6A). The out-of-plane peaks measure the distance between lattice planes parallel to the plane of the substrate; these planes should most effectively couple to out-of-plane flexing of the nanoscale pores. As the splitting in this peak arises from the rhombohedral distortion in BFO, a decrease in splitting indicates that the rhombohedral angle is tending back toward 90^{o}.

The results above can by described as anisotropic strain state in-plane versus out-of-plane in the mesoporous sample. Mesoporous samples prior to electrical poling show an amplified magnetic moment over that of the dense prior to electrical poling. Samples with ordered pores upon poling show an even larger amplification of their magnetic moment as a result of the anisotropic strain introduced into the system. It is important the note that the dense sample does not show an initial amplification of magnetism nor amplification after electrical poling. This result is due to the dense samples not being under strain. Conversely disordered porous samples have an initially amplified magnetism but show no difference upon electrical poling. Therefore, it is important to have some order in the system to allow the pores to flex and create further strain states in the system. Recent work by He et al. has also confirmed that highly distorted systems result in amplified magnetism [88]. Here we show control over the over net magnetization of BFO through electric field induced strain.

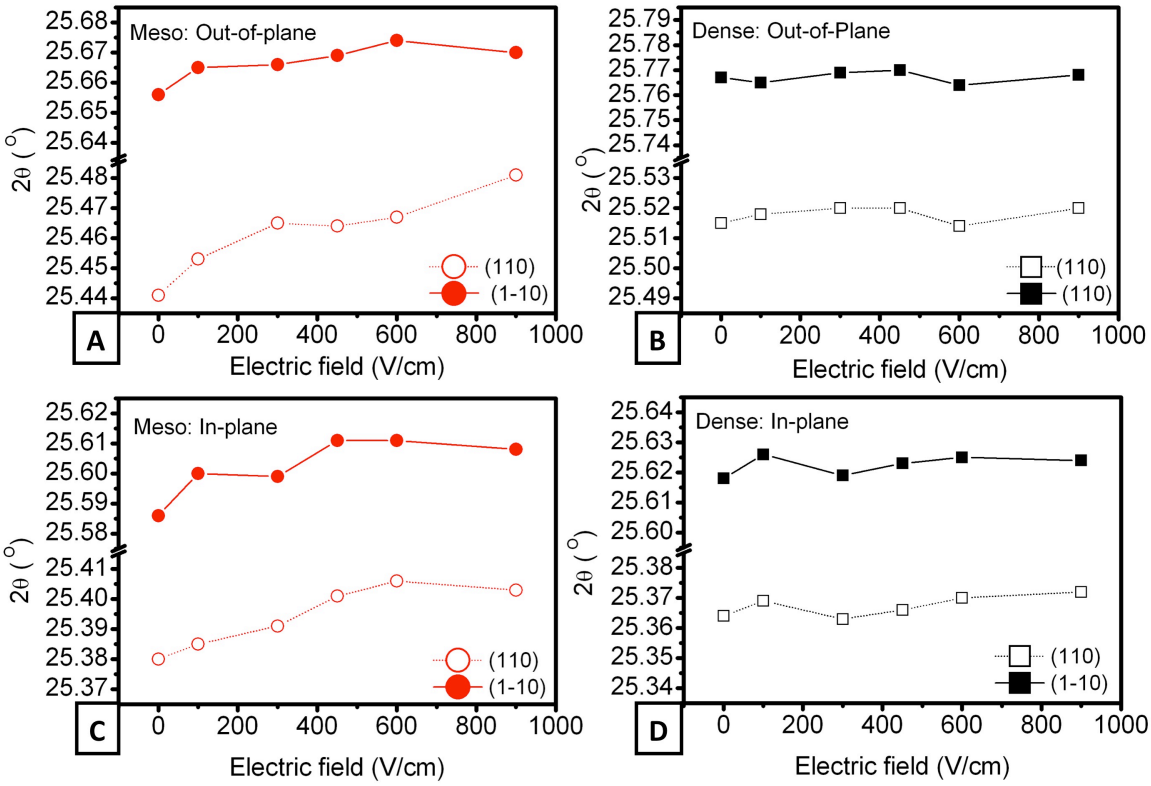

Figure. 4.6 High angle synchrotron experiments displaying the shifts in peak position for out-of-plane (A, B) and in-plane (C, D) (110) and (1-10) lattice planes as a function of electric field (circles and squares represent ordered mesoporous and dense BFO, respectively, open and closed symbols represent (110) and (1-10) planes, respectively. The results suggest the crystal lattice contracts upon electrical poling in the mesoporous BFO. Separation of the (110) & (1-10) peaks for out-of-plane mesoporous BFO decreases upon electrical poling, suggesting a decrease in the rhombohedral distortion (A). (All data reported in Cu K-alpha 2theta).

	slope (100) * 10^{-5}		slope (110)* 10^{-5}		slope (1-10)* 10^{-5}	
Dense: Out-of-Plane	-0.48	±0.86	0.27	±0.46	0.10	±0.42
Dense: In-Plane	0.02	±0.58	0.99	±0.52	0.46	±0.55
Meso: Out-of-plane	0.85	±0.62	4.83	±0.82	1.78	±0.69
Meso: In-Plane	1.05	±0.83	3.60	±0.82	2.89	±1.2

Table 4.1 Slopes obtained from linear fits of 2theta values obtained from (100), (1-10), (110) planes of mesoporous and dense BFO films upon electrical poling. Graphical representation of this data can be see in figure 3. The larger slopes of the mesoporous samples describe a shift to higher 2theta resulting in contraction of the lattice (smaller d-spacing), much larger than the dense samples.

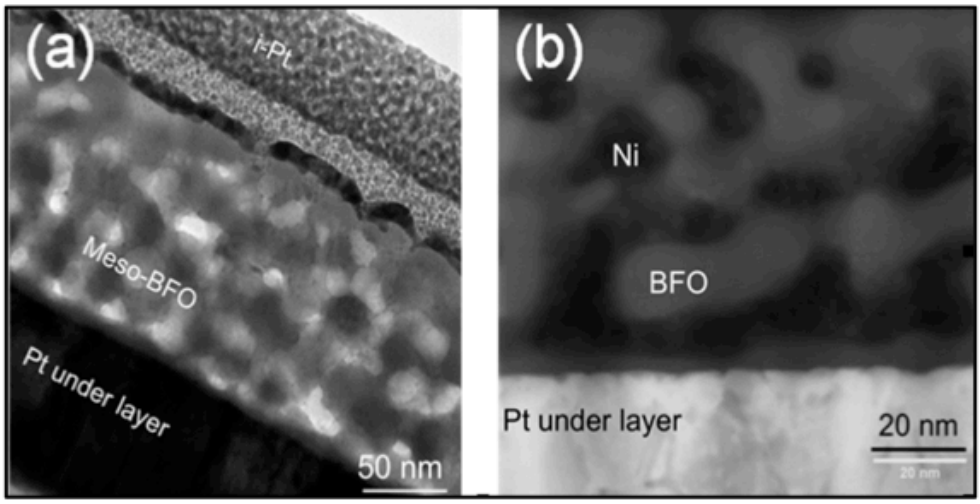

Figure. 4.7 Electroplating of nickel into the porous framework is possible as viewed by high angle annular dark field STEM images revealing homogeneous nickel incorporation. A lower magnification image is shown in (a) and a high resolution image, demonstrating complete pore filling, is shown in (b). These steps show the feasibility of forming composite materials based on nanoporous materials.

We show above that porosity provides a powerful way to strain engineer nanostructured materials. The high surface area of nanoporous materials also provides an opportunity to create intimately mixed composite materials, as the pores can play host to a myriad of materials. As an example, mesoporous BFO films fabricated on conducting platinized silicon wafers were electroplated with a ferromagnetic nickel phase. The electroplating technique successfully filled the pores and was non-destructive as evidenced by HRTEM and energy dispersive experiments (Figure 4.7). This proof-of-principal experiment lays the foundation of future work aimed at realizing intimately mixed composite materials [96–99] based on mesoporous frameworks.

4.3 Conclusions

Facile production of BFO materials with electrically switchable enhanced ferromagnetism in thin film format could be beneficial for a range of applications[8,82,83,100]. Porous materials offer interesting potential to strain engineer magnetoelectric materials using wet chemical methods without the need for expensive epitaxy. Strain induced by porosity can be reproducibly generated and can be tuned, though not with the precision of epitaxial films [87], by relaxing the strain in the system through extended thermal annealing [5]. The observation of electrically induced changes in strain and M_S in porous BFO further demonstrate novel magnetoelectric coupling not previously observed in dense epitaxially strained materials. This work thus adds to a growing body of results indicating that strain is the key to converting antiferromagnetic BFO into a useful ferromagnetic magnetoelectric material.

4.4 Experimental

4.4.1 Materials and Synthesis

$Bi(NO_3)_3$ x $5H_2O$ (99.9%) and $Fe(NO_3)_3$ x $9H_2O$ (99.9%) were purchased from Sigma Aldrich and used without further purification. $H[(CH_2CH_2)_{0.67}(CH_2(CH)CH_2CH_3)_{0.33}]_{89}$-$[OCH_2CH_2]_{79}OH$ (refered to as KLE-22) was used as the organic template. For a typical synthesis of mesoporous BFO a scintillation vial was charged with $Bi(NO_3)_3$ x $5H_2O$ (0.371 g), $Fe(NO_3)_3$ x $9H_2O$ (0.310 g) and 2 mL anhydrous 2-methoxyethanol and allowed to stir for several hours. In a separate vial the diblock copolymer KLE-22 (0.085 g) was added to 1 mL ethanol and heated to 50^{o}C until completely dissolved. The two solutions were combined into a single vial and allowed to stir for a further 2 hours, filtered and were ready for deposition. Films were deposited via dip coating in a humidity controlled environment (25 – 25%) at varying withdrawal rates (between 1 and 2 cm/s) depending upon desired film thickness. Once deposited the films are heated in air from 50^{o}C to 180^{o}C over a 3 hour period, and are allowed to soak for 12 hours. To achieve crystallization of the mesoporous films further annealing is required, the films are heated in air to 475^{o}C at 4^{o}C/min, soaked for 1min and removed immediately.

4.4.2 Methods

In- and out-of-plane high angle X-ray diffraction (XRD), 2D small angle X-ray scattering (2D-SAXS), FESEM, and SQUID magnetometry were conducted to characterize the samples. Conventional high angle XRD was measured using a D8-GADDS diffractometer from Bruker instruments (Cu-K_α radiation). 2D-SAXS and angular-dependent high angle XRD data were collected at the Stanford Synchrotron Radiation Laboratory using beam lines 1-4 and 7-2, respectively. FESEM images were obtained using a JEOL 6700F instrument. Magnetic measurements were carried out on a Quantum Design MPMS 5T SQUID magnetometer with

RSO detection. Site-selective cross sectional TEM sample preparation was performed using an Omniprobe lift-out on a dual-beam FEI Strata 400 focused ion-beam (FIB). All high resolution transmission electron microscopy (HRTEM) and high angle annular dark field (HAADF) scanning transmission electron microscopy (STEM) were performed on a JEOL 2100 operating at an accelerating voltage of 200 kV. Piezo force microscopy (PFM) measurements were performed on a Dimension 5000 system operating in DC mode.

CHAPTER 5

Magnetoelectric Control of Superparamagnetism

5.1 Introduction

Electromagnetic devices, including antennas, motors, & memory, rely on extrinsic coupling produced by passing an electrical current through a wire to generate a magnetic field, a discovery made by Oersted and further developed by Ampere in 1820[101]. While extremely successful in the large scale, this approach suffers significant problems in the small scale where resistive losses are preventing further device miniaturization. Since Curie's first attempt in 1894[4], researchers have searched for an intrinsic approach to electrically control magnetization and some minor progress has been made during the last decade using electric field induced strain to modulate magnetization in multiferroic composite materials.[102–104] While promising, these "bulk" multiferroic materials contain multi-domain magnetic structures that produce marginal magnetization changes with the application of an electric field.[105–109] During the last five years, a handful of researchers have focused on nanoscale elements, using electric field induced strain to control a single magnetic domain.[3,6,7,110,111] These studies show more dramatic magnetization changes, but the electric fields only reorient the magnetization state and do not change its magnitude. Therefore, what is critically needed is an approach to intrinsically control the net observed magnetization state. Superparamagnetism, which occurs in nanoscale ferromagnetic crystals when the ambient thermal noise is larger than the magnetic ansisotropy resulting in a zero magnetization state, may hold the solution to this problem.[112–114] Here we report experimental results demonstrating that an electric-field-induced anisotropy in a multiferroic

system is capable of electrically switching between a superparamagnetic state and a single-domain ferromagnetic state at constant temperature and thus represents an intrinsic approach to turn on and off a net magnetic field. This electrical modulation of magnetism is achieved via an electric-field-induced strain in a magnetoelectric composite composed of Ni nanocrystals mechanically coupled to a (011) oriented PMN-PT single crystal. To our knowledge, this is the first example of a system where an electric field is used to turn on and off a permanent magnetic moment, and thus this work marks a significant advance in the field of electromagnetic devices.

5.2 Results and Discussion

5.2.1 Synthesis of Ni Nanocrystals and Preparation of Ni Nanocrystal PMN-PT Composite

The magnetoelectric composites used in this work were composed of ferromagnetic 16 nm diameter Ni nanocrystals mechanically coupled to (011) $[Pb(Mg_{1/3}Nb_{2/3})O_3]_{(1-x)}$-$[PbTiO_3]_x$ (PMN-PT, x≈0.32) ferroelectric single crystal substrates. Nickel was chosen for its great magnetoelastic properties as well as its stability in comparison to other pure magnetoelastic metals. The nanocrystals were synthesized via thermal decomposition of 1 mmol Nickel acetylacetonate in the presence of oleyamine (7 ml), oleic acid (2 mmol), and triocylphosphine (2 mmol).[115] For this work, optimized conditions for the synthesis varied slightly from ref 19 and are thus summarized here. The solution was stirred at room temperature for 20 minutes under gentle Ar flow before heating first to 130°C for 30 min, and then to 240°C (reflux) for 30 min. The solution was then cooled, and the particles were precipitated with ethanol and centrifuged. Two further washings were done with ethanol and hexane followed by centrifugation to remove any unbound ligands. The particles were stored dissolved in hexane under Argon.

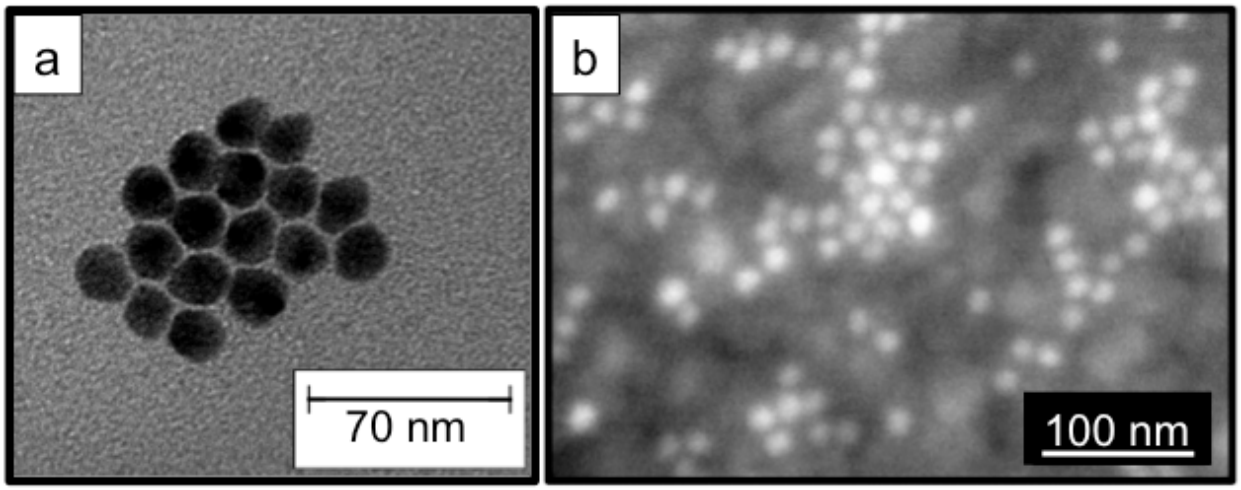

Figure 5.1. Characterization of Ni nanocrystals. Part **a** shows a TEM image of several as-synthesized Ni nanocrystals. The average nanocrystal diameter is ~16 nm and particles are approximately spherical and non-agglomerated. Part **b** shows an SEM micrograph of the nanocrystals after deposition onto the piezoelectric substrate. Sub-monolayer coverage of non-agglomerated nanocrystals is observed.

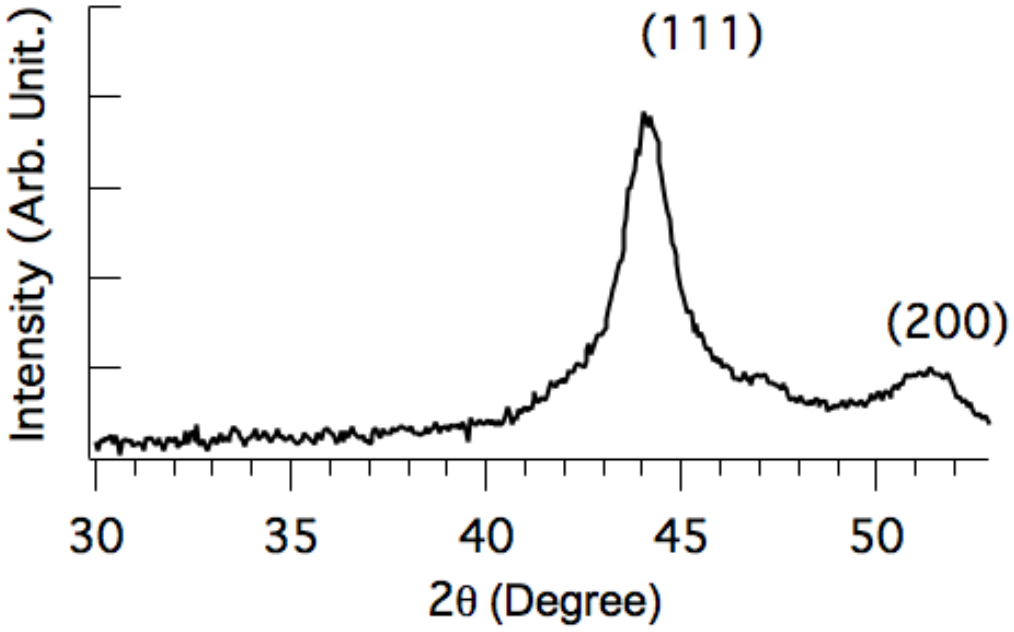

Figure 5.2. Powder XRD obtained on as synthesis Ni nanocrystals. Peaks correspond to the FCC crystal structure of Ni and peak positions are in agreement with JCPDS card #4-850.

Deposition of Ni nanoparticles onto PMN-PT substrates was done using a slow evaporation technique.[116] The (011) oriented PMN-PT single crystal ferroelectrics were manufactured by Atom Optics CO., LTD. (Shanghai, China). The substrate was angled between 60-70° in a vial containing a dilute solution of Ni nanocrystals dispersed in hexanes. Gentle heat of approximately 80°C was applied to facilitate evaporation along with a gentle Ar flow to prevent oxidation of the Ni nanocrystals. Argon plasma etching and Pt sputtering was done using a Hummer 6.2 from Anatech.

Figure 5.1a shows TEM images of the as-synthesized Ni nanocrystals indicating that they are both spherical and fairly monodispersed in size. X-ray diffraction data obtained on the Ni nanocrystals (figure 5.2) shows an FCC structure (JCPDS #4-850), consistent with literature reports. Magnetoelectric composites were produced by slowly evaporating a dilute solution of the Ni nanocrystals dissolved in hexane onto an unpoled PMN-PT substrate coated with a thin titanium adhesion layer in an Ar atmosphere.[116] An SEM image of the particles deposited onto the substrate is shown in figure 5.1b, demonstrating that a homogeneous sub-monolayer distribution is produced. The organic ligands on the particles were subsequently removed in an inert atmosphere using a two minute argon plasma etch. Without breaking vacuum, a 30 nm thick Pt layer was deposited onto the PMN-PT substrate to fully encase the Ni particles and protect them from oxidation (see figure 5.3a). The Pt layer also provides a load transfer path from the PMN-PT substrate to the Ni nanocrystals. A schematic of the complete magnetoelectric architecture is shown in figure 5.3a. XPS depth profiling analysis (figure 5.4) of the magnetoelectric composite indicates that the Ni nanoparticle are well preserved throughout this process, and that only a small amount of oxidation occurs (XPS Ni 2p peak analysis shows 95% Ni, 5% NiO).

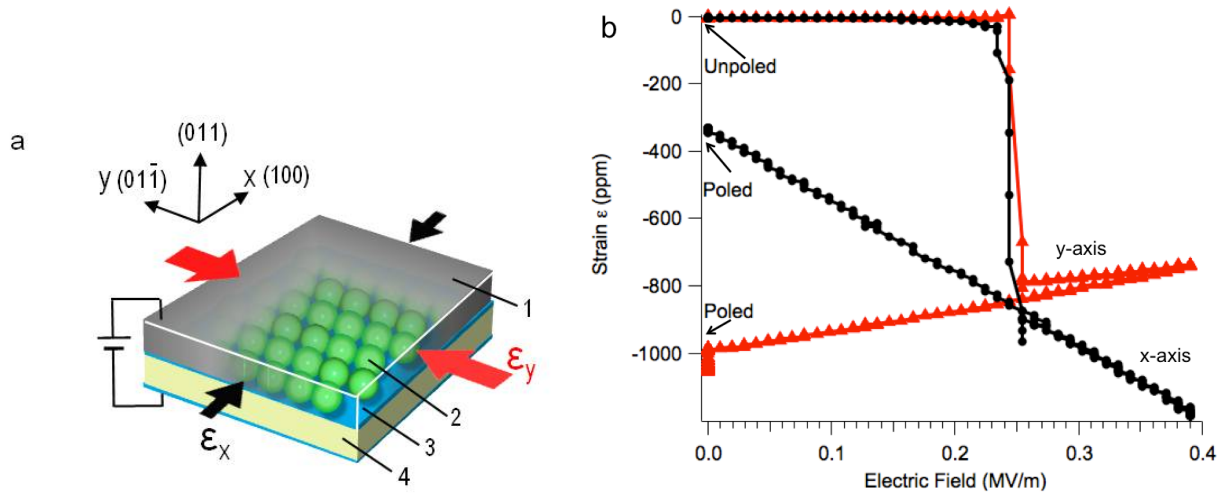

Figure 5.3. Magnetoelectric device characteristics. Part a shows a schematic representation of the full device. **1**: 30 nm thickness Pt layer (drawn partially transparent for clarity). **2**: 16 nm diameter Ni nanocrystal. **3**: 10 nm thick Ti electrodes evaporated on the top and bottom of the PMN-PT. **4**: 500 μm thick (011) oriented PMN-PT single crystal substrate. . Arrows indicate the direction of induced anisotropic strain. Part **b** shows the strain induced in PMN-PT via an electric field applied along the (011) direction. Red triangles indicate strain along the y-axis, black circles along the x-axis.

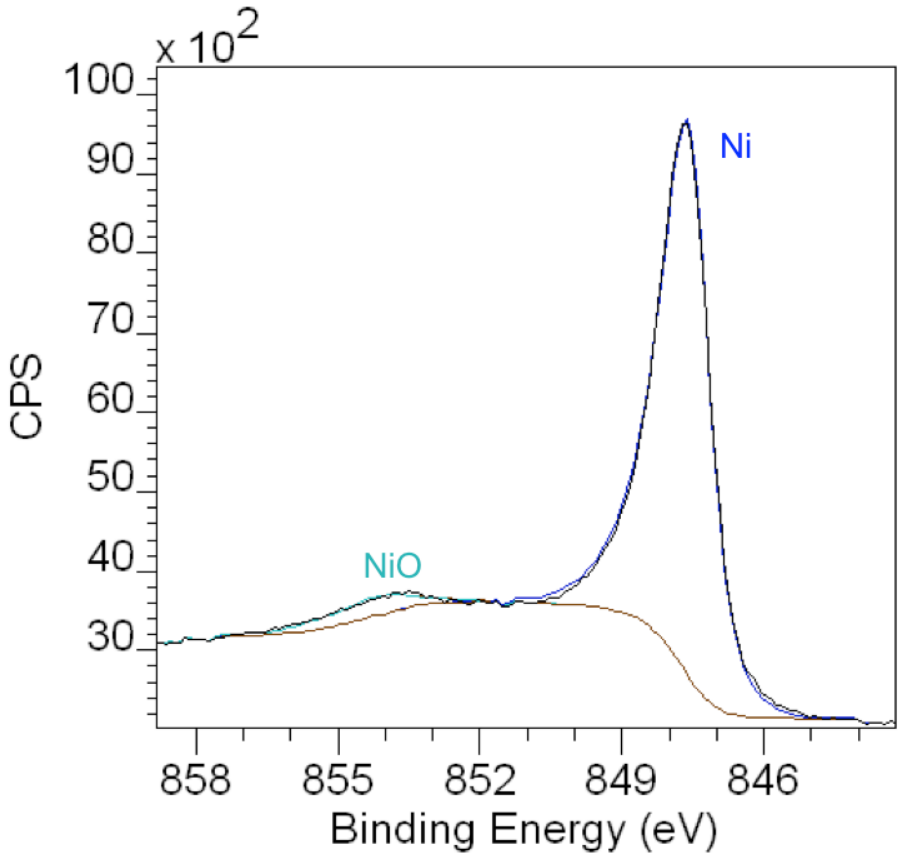

Figure 5.4. XPS depth-profiling data on Ni nanocrystals embedded in Pt on top of a PMN-PT substrate. For this data, Ar ion etching was used to remove the top Pt layers of the sample, exposing the Ni nanoparticles. The data show only minimal oxidation of the Ni nanocrystals embedded in the Pt; fitting of the Ni 2p peaks gives 5% NiO and 95% Ni. The NiO peak is indicated by the light blue trace and the dark blue trace indicates the Ni metal peak, the raw data is shown in black.

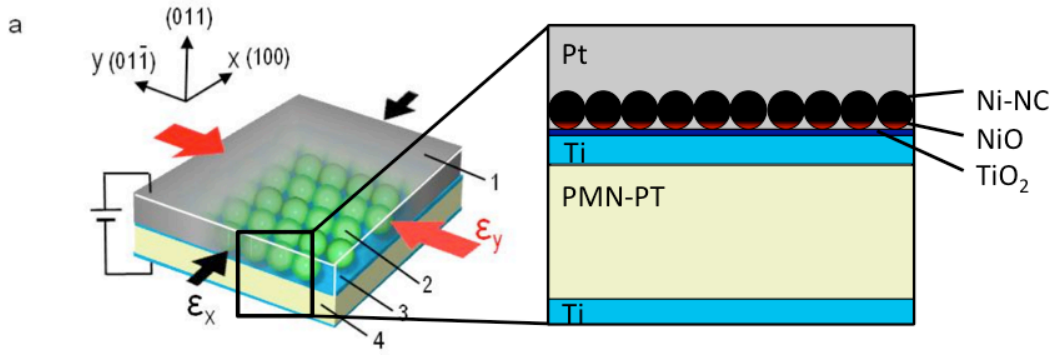

Figure 5.5. Magnetoelectric device characteristics. (Left) A schematic representation of the full device. **1**: 30 nm thickness Pt layer (drawn partially transparent for clarity). **2**: 16 nm diameter Ni nanocrystal. **3**: 10 nm thick Ti electrodes evaporated on the top and bottom of the PMN-PT. **4**: 500 μm thick (011) oriented PMN-PT single crystal substrate. . Arrows indicate the direction of induced anisotropic strain. (Right) A more detailed schematic of the adhesion of Ni nanocrystals to the substrate. The evaporated Ti electrode will oxidize to TiO_2; deposited Ni nanocrystals oxidize slightly to NiO when deposited on TiO_2 creating adhesion between the NiO and the TiO_2 surface.

This slight oxidation of the Ni nanocrystals allows for good adhesion to the surface of the substrate through the NiO bond formation. A more detailed schematic of this can be seen in figure 5.5. This adhesion is required to allow strain transfer into the particles resulting in magnetoelectric coupling. When the nanocrystals are deposited on Pt substrates to prevent any oxidation from occurring the effects reported in this paper are not seen suggesting oxide bond formation is required to create proper adhesion.

5.2.2 Magnetometry Analysis of Ni Nanocrystal PMN-PT Composites

Magnetic measurements on the magnetoelectric sample were performed before and after poling the PMN-PT substrate at room temperature. Figure 5.3b shows the anisotropic in-plane (x-y plane) strains generated as a function of applied electric field measured using a bi-directional strain gauge attached to the sample. In the unpoled state, the Ni particles in the magnetoelectric sample are subjected to negligible strains ($\varepsilon_x=\varepsilon_y=0$). During poling (i.e. E=0.4 MV/m), compressive strains up to ε_x=-1200 με and ε_y=-800 με are produced. Upon removal of the electric field, large anisotropic compressive strains of ε_x=-300 με and ε_y=-1000 με are present in the poled state. Since Ni has a negative magnetostriction coefficient, any induced magnetoelastic anisotropy causes the magnetic dipoles in the single domain Ni nanocrystals to align along the dominant compressive strain direction (which corresponds to the deeper energy well).[7,117] For the poled state, the larger anisotropic strain along the y-axis direction produces this deeper energy well.

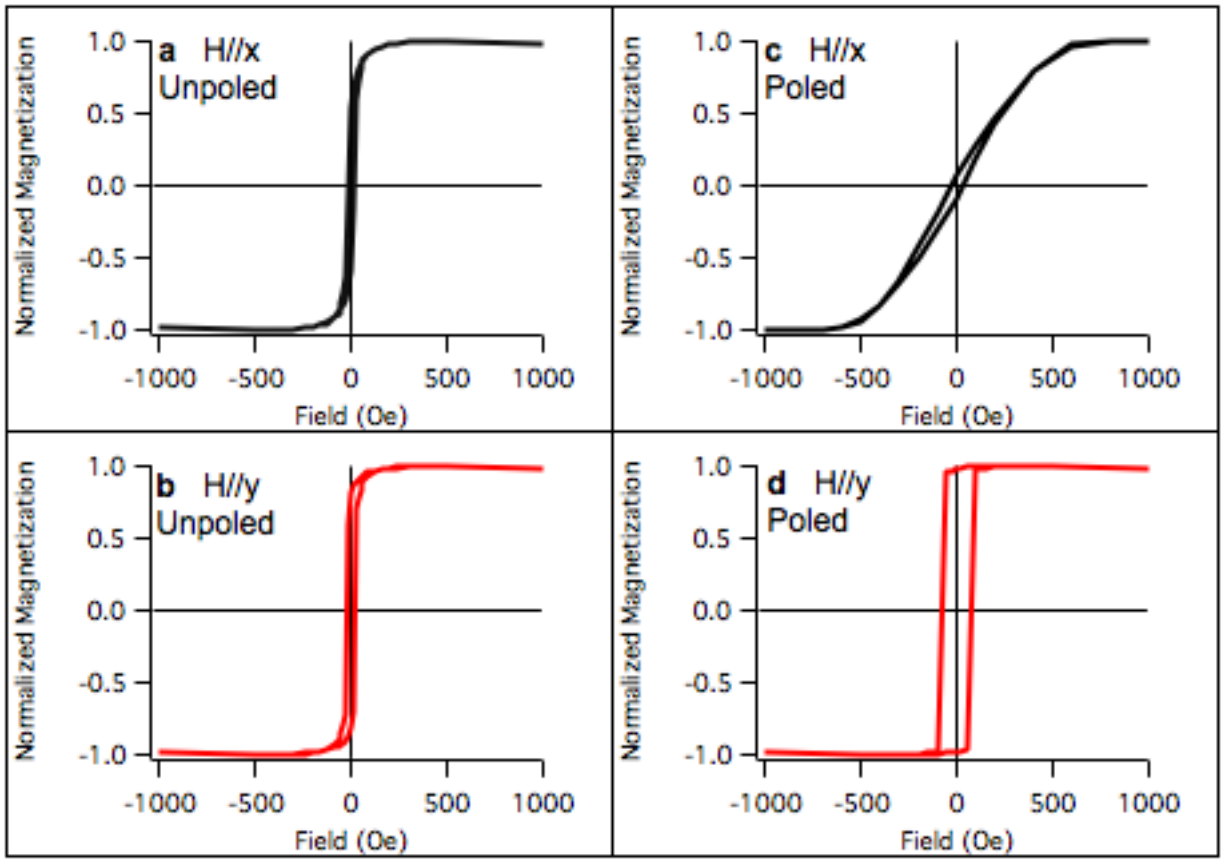

Figure 5.6. Magnetic hysteresis curves obtained on nickel nanocrystals embedded in Pt thin film on top of (011) PMN-PT at 298 K. Parts **a**, **b** show data measured with the magnetic field applied parallel to the x- and y-axes, respectively on the unpoled sample. Parts **c**, **d** show data measured with the magnetic field applied parallel to the x- and y-axes, respectively on the poled sample.

Figures 5.6a and 5.6b show room temperature magnetic moment (M) measurements as a function of the applied magnetic field (H) for the unpoled (i.e. $\varepsilon_x=\varepsilon_y=0$) magnetoelectric composites measured in x- and y-directions, respectively. Measurements were conducted using a superconducting quantum interference device (SQUID, Quantum Design, MPMS XL-5). Similar, small coercive fields, $H_c < 20$ Oe, are observed in both directions indicating that the sample is both magnetically isotropic in-plane and dominantly superparamagnetic (i.e. they show near zero net magnetization). The small anisotropies observed are attributed to small variations in the spatial distribution of nanocrystals produced during the evaporative deposition process used to manufacture the magnetoelectric composite and are typical of magnetic measurements on arrays of superparamagnetic nanocrystals. Figure 5.6c and 5.6d show similar magnetic measurements on the poled (ε_x= -300 με, ε_y= -1000 με) magnetoelectric composite. The data in figure 5.6c shows a hard magnetic axis is created parallel to the x-direction for the poled sample with a magnetic anisotropy (H_a) of 600 Oe. The ratio of the remanent magnetization (M_r) to the saturation magnetization (M_s) is very low, suggesting that domains tend to orient in an off-axis direction. In contrast, figure 5.6d shows a magnetic easy axis is created along the y-direction for the poled sample. In this direction, M_r is approximately equal to M_s, indicating that the sample consists of essentially single domain Ni nanocrystals that are aligned along the y-axis. Furthermore, H_c=80 Oe measured along this direction confirms a deeper potential well for spin alignment is present in the y-direction after application of an electric field. This result thus demonstrates that the application of an electric field stabilized the y-axis aligned spin state, resulting in a net magnetization equivalent to the saturation magnetization of Ni (i.e. 485 emu/cc).

Rephrased, this result shows that we can us an applied electric field to "turn on" a net magnetization.

Figure 5.7a and 5.7b show normalized magnetic moments as a function of temperatures for the unpoled magnetoelectric sample. Samples were initially cooled to 10 K in the absence of a magnetic field (zero field cooling, ZFC) followed by measurement of the magnetic moment as a function of temperature in a 50 Oe applied field. The temperature corresponding to the highest magnetic moment is typically defined as the blocking temperature (T_b), above which magnetic dipoles begin to lose their directionality due to thermal randomization and the sample becomes superparamagnetic.[118] There are some small differences in the data measured in the x- and y-directions, which are attributed to the evaporative deposition process, as discussed previously. Nonetheless, similar blocking temperatures of ~300 K are found in the unpoled state in both directions. By contrast, figures 5.7c and 5.7d show ZFC curves for the poled magnetoelectric sample measured along the x- and y-directions, respectively. The data measurements in the x-direction (hard axis) shows a peak at 280 K, which represents a decrease of 20 K compared to the peak observed in the unpoled samples (Fig 5.6a and 5.6c). More dramatically, for the y-direction (easy-axis) the peak of the magnetization curve (or T_B) increases to 340 K, or a change of 40 K when compared to the peak in the unpoled samples.

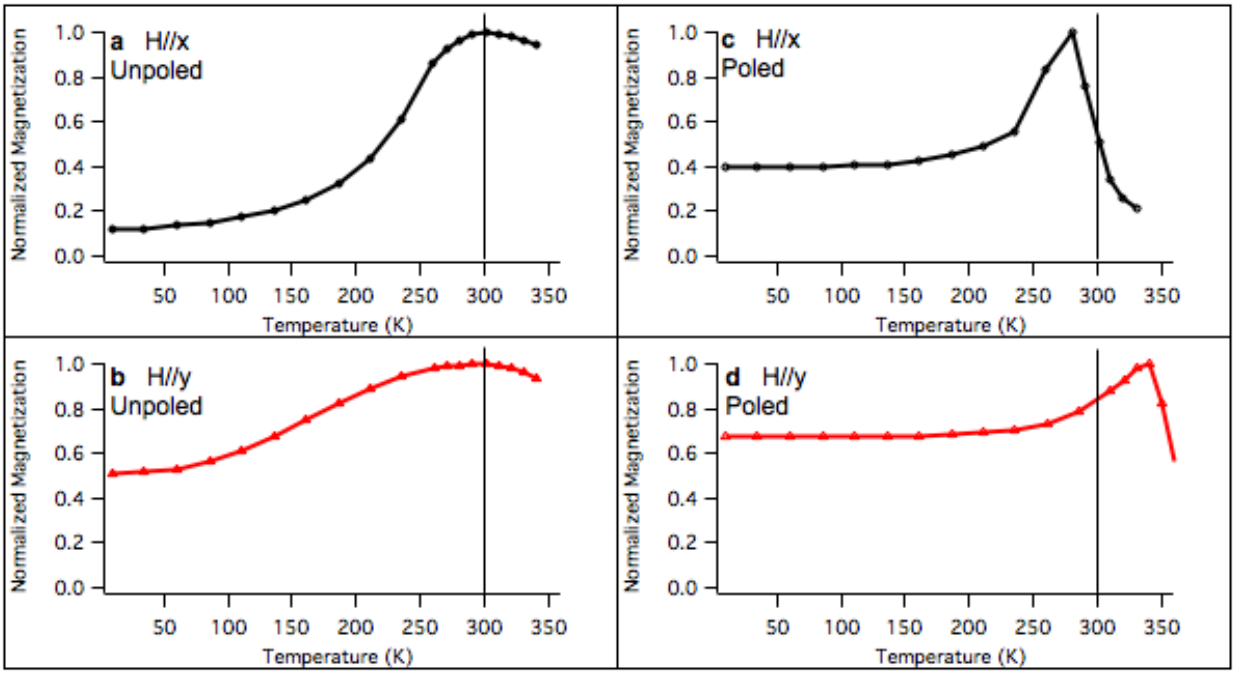

Figure 5.7. Zero field cooled (ZFC) magnetization curves as a function of temperature for Ni nanocrystals embedded in Pt on (011) PMN-PT before and after electrical poling. All data is normalized to 1 at the peak magnetization. Parts **a** and **b** show data on the unpoled sample, measured in the x- and y-directions, respectively. Parts **c** and **d** show data on the poled sample, again measured in x- and y-directions, respectively. All curves were measured using a 50 Oe applied field. The line drawn at 300K is intended as a guide to the eye.

5.2.3. Theoretical Analysis

The shifts in the maximum of the ZFC curves can be explained by considering how the potential landscape for spin alignment is changed in an anisotropically strained sample. In the unpoled sample, the magnitude of the barrier for spin flip is on the order of the available thermal energy at room temperature and so the spins begin to hop between magnetic easy axes as the blocking temperature of 300 K is approached. When the sample is anisotropically strained by the PMN-PT substrate, however, the potential well for spin alignment in the y-direction is deepened. It thus requires significantly more thermal energy for the spins to hop out of this deeper well, and so the blocking temperature shifts to well above room temperature (340 K) after electric poling. In the x-direction, the blocking temperature appears to decrease, but this is not a true blocking temperature, as the fall-off in magnetization at 280 K is not thermal randomization of magnetic moments, but rather magnetization transfer from the x-direction to the y-direction as the system obtains sufficient thermal energy to free the spins from the metastable potential minima where they were trapped. Because spins are directionally transferring from a high energy configuration to a lower energy configuration, the process occurs at a lower temperature than the thermal randomization observed in the unpoled sample. The true blocking temperatures in the unpoled and poled system are thus 300 and 340 K respectively. This result thus confirms the experimental results shown in Figure 5.6, which indicate that the electric field can be used to stabilize the ferromagnetic spin state at room temperature. This is accomplished by moving the blocking temperature from a value very near room temperature, to a value well above room temperature

The above conclusions can be validated using the Arrhenius-Neel equation, $\frac{1}{\tau} = \frac{1}{\tau_0} e^{\frac{-KV}{k_B T}}$, where τ is the magnetization switching time, K is total anisotropy energy density, V is particle volume, k_B is Boltzman's constant, T is the temperature, and $\frac{1}{\tau_0}$ is the attempt frequency. Using $\frac{1}{\tau_0}$ $=10^9$/second and τ = 100 seconds produces the familiar $KV=25k_BT$ relation.[119,120] For this system, the electric-field-induced change in the magnetoelastic anisotropy is approximated by $\frac{3}{2}\lambda Y \Delta\varepsilon_a$, where λ= -34 με is the Ni magnetostrictive constant, Y=213.7 GPa is the Ni Young's modulus and $\Delta\varepsilon_a$=–700 με is the residual strain induced in the Ni nanocrystal after electric poling (see figure 2b).[7,117] Incorporating this anisotropy term into the Arrhunius-Neel equation produces $\frac{3}{2}\lambda Y \Delta\varepsilon_a = 25k_B\Delta T_B$, which provides an estimate of the blocking temperature change ΔT_B that should result from the additional magnetoelastic energy added during electric poling. The calculated value of 46 Kelvin is in excellent agreement with the measured value of ~40 K.

While the primary impact of this work lies in the fundamental abilitly to control not only the direction, but also the magnitude of a spin state using an electric field, it also has significant ramification to the miniaturization of a wide class of electromagnetic devices. Consider, for example, Magnetic Random Access Memory (MRAM), which currently faces two major engineering challenges to reduce size: overcoming the thermal instability associated with nanoscale magnetic elements and reducing the write energy to encode a bit of information.[100,121–123] In the former case, the superparamagnetic transition behavior defines the smallest bit size[112–114,124] while for the latter case, larger write energies require larger fields and thus larger write heads or other routes to reduce fields.[2] The multiferroic system discussed here offers a solution

to both of these problems, which would yield further miniaturization. By electrically increasing the magnetic anisotropy, as demonstrated in this paper, the minimum size of a stable bit of information can be reduced. Furthermore, since the magnetic anisotropy is electrically generated, the anisotropy can be modulated using an electrical field, thus providing an avenue to create bits that are magnetically hard and thus thermally stable when written, but can be electrically swicthed to a magnetically soft state that is easy to reorient for the write process. To see this process more concretely, consider the data in figure 5.6d, which shows a coercive field of the poled sample is H_c=80 Oe, corresponding to the stabilized nanoscale bit. Examination of figure 5.3b indicates that application of a 0.24 MV/m electric field reduces the magnetoelectric anisotropy to zero (i.e. $\varepsilon_x = \varepsilon_y$ or $\Delta\varepsilon_a = 0$), returning the sample to near the superparamanetic state (H_c<20 Oe). A transient bias can thus be used to reduce anisotropy during the write step. In this way, this fundamental research provides an electrical mechanism to both increase the blocking temperature, and decrease magnetic write energies, a combination that is simply not possible in conventional magnetic systems.

5.3. Conclusions

By applying electric-field-induced strain to the ferromagnetic nanocrystals, we demonstrate that superparamagnetic Ni nanocrystal with no permanent magnetic moment at room temperature can be converted to strong single-domain ferromagnets, again at room temperature, through application of an electric field. This work thus provides a revolutionary new approach for controling magnetisim at the small scale and is a sharp departure from Oersted and Ampere's original work running current through a wire. The intrinsic control of magnetization demonstrated in this paper manifests itself as an electric field induced shift in the

blocking temperature of approximately 40 degrees Kelvin for 16 nm Ni nanocrystals. Such control in a nanoscale magnetic materials may provide exciting opportunities to explore new types of electromagnetic devices as well as allowing researchers to transition conventional devices down to lengthscales too small to effectivly exploit standard electro-magnetic coupling.

CHAPTER 6

Conclusion

The work presented here shows the effects nanoscale architecture can play on magnetic and magnetoelectric materials. Here solution phase self-assembly is utilized to create a variety of structures that allows for a fundamental study on how the materials' properties can be tuned and controlled. Solution phase processing presents an efficient and less expensive way to create implement these materials into device-like architectures.

Electrochemical deposition is shown to be a very reproducible method for creating nanostructures of various aspect ratios. Though the systems presented here have little hope of being a functional spin valve device, the fundamental physics presented does show that there are interesting new architectures that can be explored compared to the conventional system. By taking advantage of the strong effects of magnetic shape anisotropy in nanoscale elements, we could study one of these exciting new systems. It is shown that because the spacing of elements can be very easily controlled during deposition, one can tune the ease of magnetic spin flips. The reproducibility and materials versatility of electrochemical deposition also makes these systems interesting for future studies.

We further studied magnetic coupling in magnetic nanocrystals. FePt nanocrystals provided an ideal system for coupling studies since they can be made both ferromagnetic and superparamagnetic at the same size due to annealing temperatures controlling the final crystal structure. By depositing these magnetic nanocrystals onto block copolymer directed self-assembled substrates, it provided a way to organize nanocrystals over larger areas without

expensive lithographic techniques. The templates prepared also benefit from an atomic layer deposition process, which allows for tuning of the trench width and increased thermal stability. The tunability of these templates allows for organization of one-dimensional arrays of nanocrystals or many nanocrystals depending of the trench width, meaning that it can be extended beyond just the proposed FePt nanocrystals. If larger or smaller nanocrystals are to be used, the trenches can be tuned to be commiserate with a variety of nanocrystals. Additional coupling can be studied on these systems; mixtures of ferromagnetic and superparamagnetic systems could lead to further understanding of the coupling along the chains studied here. Shape anisotropy could be explored by using magnetic nanorods and nanocrystals to study how they couple together in 1D trenches. A final benefit to the methods described here is the thermal and solution phase robustness of the templates. Though the systems studied here were limited to magnetic nanoparticles there could be application for other functional nanoparticles organized in such a fashion.

Block copolymer self-assembly is not limited to lamellar type organization purely for templates. Nanoscale porosity can be created by using evaporation induced self-assembly of block copolymers and soluble inorganic precursors. It is shown that the porosity created in these systems has large effects on the magnetoelectric effects of bismuth ferrite (BFO). Similar strain effects have been seen in epitaxial systems; however, the strain in those systems is limited as the strain relaxes as one moves away from the interface. In the porous system, it is able to flex and strain throughout the whole film and is not limited to interfacial lattice mismatches. Upon electrical poling the porous systems flexes and strains resulting is greater spin canting and huge enhancements of magnetization. Interestingly, when the long-range order of the pore system is

broken down and the strain in the system is relaxed the enhancement of magnetoelectric response also breaks down.

Since the chemistry that creates these porous architectures is independent of the inorganic precursors used these systems have great versatility. As the study of magnetoelectric materials grows there is an ever-increasing pool of new magnetic and magnetoelectric materials being created. It has been found that strain plays a large role in the global properties of these types of materials. The ability of these porous films to flex creates interesting strain systems and provides a great platform for different types of control of the materials properties.

Finally, composite magnetoelectric systems are explored. By using a bulk piezoelectric substrate (PMN-PT) strain is applied to magnetostrictive Ni nanocrystals. Here for the first time, it is shown that one can convert from the superparamagnetic state with no overall net magnetization to a ferromagnetic state with permanent magnetic moment at a fixed temperature. Essentially turning a system from an off to an on state. This result is very exciting as often the superparamagnetic size limit has been seen as a challenge to over come when controlling magnetization since the properties of a material change drastically when reaching smaller size limits. Additionally the geometry of the sample allows for different magnetic phases to be used. Nickel is a simple system to work with at first but is not the champion of magnetostrictive materials. Other materials, cobalt ferrite for example, have much higher magnetostrictive constants and theoretically would show much larger shifts in the superparamagnetic/ferromagnetic transition than nickel. The versatility of this system provides a vast array of new systems to study to optimize these effects.

Another challenge to overcome in this composite is the reversibility of these effects. It is believed that since the strain of the piezoelectric phase is reversible the magnetic transition

shown here can be reversed. There are two routes to possibly make this happen: depole the piezoelectric by applying a negative electric field or by applying an in-situ field the piezoelectric can reach an isotropic strain state.

Taken together the work here shows many different effects nanoscale architecture can have on magnetic and magnetoelectric systems. All of the materials discussed here have possible applications in various magnetic and magnetoelectric devices such as memory and antenna; however, building these systems into working devices will require additional research and engineering. The main purpose of this work is to provide the community with materials that have tunable properties for incorporation into devices. Often the challenge when creating a device that utilizes magnetism is the control over the magnetic moment of the material. It is shown that by carefully controlling the architecture of known materials it is possible to create systems with novel and exciting magnetic and magnetoelectric properties.

APPENDIX A

Characterization information for SQuID magnetometry, and XPS; Detailed synthesis conditions for mesoporous thin films and block co-polymer trenches

The first section describes the protocols for two different measurement techniques; SQuID magnetometry, and XPS. Sample mounting, and analysis is focused on in this section. Additionally detailed synthetic conditions for mesoporous thin films of CFO is detailed along with step by step conditions to create nano trenches from PS-b-PSDMS block co-polymers.

A.1 Sample mounting and analysis of SQuID magnetometry

Two main types of samples can be prepared for the SQUID: (1) powder samples, and (2) thin films. All samples should be mounted approximately 10 cm from the top of the straw. (1) Powder samples should be placed into a pill capsule and mounted into the straw by poking holes above and below the capsule. If the least interaction between particles is desired they should be mounted in wax prior to deposition into the sample. To mount in wax a small portion (1-2 g) of wax is placed in a vial on a hot plate ~ 120°C, once the wax is melted drop a few drops of the powder sample dispersed in hexanes or chloroform into the wax and swirl to combine. Once combined use a glass pipette to quickly transfer some wax into a pill capsule. Allow the wax to dry completely before mounting into the straw. Note: The wax should show only a faint color of the sample. For example if you have a black solution of nanoparticles the wax should be a very faint grey color. (2) Thin film samples should be cute square to the approximate diameter of the straw if possible (0.5 mm x 0.5 mm). Thin film samples can be mounted either parallel or

perpendicular to the applied magnetic field in the SQUID. The field is applied parallel the to the long axis of the straw. For samples mounted parallel to the magnetic field if cut to the size of the straw they will fit snuggly into the straw when just pushed down. If the sample seems to move around the straw can be deformed slightly around the sample for a better fit. To measure the two different in-plane directions a marker should be placed on the sample to orient x vs. y. If the sample is to small to fit into the straw on its own the rounded ended of the pill capsule should be placed above and below the sample to pinch it into the place. The capsules as always should be secured with holes punched slightly above them. It is worth noting this mounting technique should only be used for samples with large signals as the addition of the capsules adds a large contribution to the diamagnetic signal. Finally the perpendicular orientation, the straw should be cut approximately 10 cm from the top. The sample is then placed between the two pieces of straw and taped back together using Kapton tape. The tape should extend at least 3 cm past the sample position, this will prevent any fluctuations in the diamagnetic signal within the measurement window (the measurement window is 4 cm).

Prior to inserting the sample into the instrument the following parameters should be checked: Temperaure at 298K, field at 0 Oe, liquid He above 40%. If all of these parameters are met click sample from the top menu and then remove (possibly insert depending on what the last user did). A pop up window will instruct you when the system is properly vented, once you see this message you may remove the servo cap and careful lower the sample rod into place. Before inserting the rod be sure the bottom portion is properly screwed into place. If you find there is resistance when trying to insert the rod inspect your sample and make sure it is not much larger than the diameter of your straw. If it is you will have to trim down and re-mount your sample. Once the servo cap is replaced press purge on the message window open on the computer, the

system will go through an automatic vent/purge cycle. During this you can click finish on the window. If desired it is recommended to insert sample information on the next window the pops up. Once done hit ok.

When along the bottom of the screen below the He level there is a read out that says "purged, ready" you may click on the section along the bottom that reads out the field value to apply a field for centering. Recommended parameters are: field 50 – 100 Oe, Approach "no overshoot", Mode "high res enabled", click set when ready. From the top menu click "center" then "RSO", on the pop up press "initialize transport", then press "center" and wait for the measurement to finish. Normally you will have to press "Adjust position" and enter "4.2" to get the center near the peak or minimum if the sample was mounted 10 cm from the top. Once you enter the position number press adjust automatically, once finished another graph will pop up with a max or min hopefully in the window, iterate "Adjust position" and "adjust automatically" until the max or min is located at 2 cm on the graph. If you find that your sample is showing a mostly flat line your sample is probably too large and is getting stuck, trim down and try again. You may also need to increase the applied field in order to get a measureable signal from your sample. Once centered you will be able to run your sample by opening up a sequence and pressing the "play" symbol along the top of the screen.

To check the fitting of the data open up the ".raw" file for the run in question. Right click on the graph and select "X1", field, "Y1", long detrended voltage, "Y1", long detrended fit. In the lower right select point 1 thru 64, you can now cycle through and see if the fits are ok. If the fits are jumping around it is possible your sample is moving and needs to be secured better. In the sequence you can also make sure you are measuring at the slowed frequency for the RSO (0.5 Hz). If you are running a magnetoelectric sample jumpy fits may need to be thrown out. If

this is the case increasing the number of cycles per data point is recommended, normally the sequences will run 3x rso, with an iterative fit. And iterative fit will find the peak center if it shifts slightly during measurement. The linear fit should only be used if a sample is secured very tightly but the signal is so noisy it is hard to get a fit as it will always assume peak center at 2 cm.

Once the raw data is confirmed as good the "rso.ndat" file can be exported into a graphing program to do final corrections. If plotting an MH curve it is possible to need to substrate off a diamagnetic signal. The diamagnetic signal creates lines with a negative slope at high fields. To remove this the linear portions of the curve at high field should be fit to a line. The slope of that line will be multiplied by the field at each data point measured, by doing this you are recreating the linear portion of the graphs that are due to diamagnetism. One must remember when doing SQuID magnetometry that the curves are the linear sums of all of the components in the sample. The calculated values can now be subtracted from the measured values. Once replotted the curves should appear flat at high fields, if this is not the case the linear fit should be redone.

A final note about the Y-axis from the SQuID, this value when given from the instrument is in emu. This value must be normalized, this can be either mass normalized for the sample or area normalized. Either are acceptable and which to use depending on the individual sample.

A.2 X-Ray photoelectron spectroscopy

This section is intended to describe the general operation of the Kratos Axis Ultra XPS system. Here general sample preparation and loading with be addressed. A section on general operation procedures is included as well as a brief introduction to sample analysis using CasaXPS.

A.2.1 Sample Preparation and loading for XPS

The XPS is a ultra high vacuum (UHV) system, for this reason all samples must be fully dried or outgassed prior to loading into the pump down chamber. Samples are mounted either on stubs or sample bars via double-sided tape or conductive copper tape. Careful care should be taken to avoid exposing any of the tape epoxy as this is bad for the vacuum system and will result in poor vacuum levels.

Prior to loading samples the user should check to make sure the flap valve between the SAC and STC is closed. When samples are ready to load the 3 screws on the STC door can be loosened and the "STC vent" sequence can be started. Once vented samples can be loaded onto the magazine. The samples have 2 possible ways to hook onto the hooks, they should be secured to the lower groove on the bar/stub. The long arm (herein referred to as the hook) should hold the top groove of the samples. Once loaded the door should be secured and the "STC pump" sequence should be started. The user should hold the door tight during the first few minutes of pumping to assure the pumping starts properly. Optimum vacuum levels will be reached overnight; however, the samples can be loaded into the SAC after 2 hours of pumping.

To load the airtight holder "safe manual mode" is used. The holder is attached to the small door on the STC and the main door of the STC is closed as described above. First the "V3 valve" is opened, and the "PG gauge" is turned on. Once the vacuum reaches 10^{-2} torr the screw on the holder can be slightly loosened letting the sample be pushed into the chamber and loaded onto the fork. After this the inert sample holder should be pulled closed and the screw secured. Double check the vacuum level is still below 10^{-2} torr. The "turbo pump" can be turned on at this point. The "STC CCD" should not be turned on for at least 15 min to allow the system to

reach ok vacuum levels. The system will take the same amount of time to pump down as described above.

To load samples into the STC the STC/SAC valve must be opened using, “STC-SAC valve open” sequence. If this fails double check the sample hook is completely retracted on the light on the cap on the end of the rod is green. If the hook is retracted and the color is red double check that the cap is in position, the light will turn red if it is not properly secured.

Once the valve is open the SAC fork, this holds the samples for analysis in the SAC, can be moved into the position. Load the position table “bars and stubs”. The top 2 positions are for loading stubs and the bottom 2 are for loading the bar. To move to a position click on the position you would like and click “go to.” The center position is where the SAC fork needs to be to load a sample from the STC to the SAC. Once in position move the samples into position with the fork. If the hook and SAC fork do not perfectly line up the controller can be used to adjust the exact heights, once secured use the left position to remove the sample from the hook onto the fork by clicking “go to” again on the table window. Jiggle the fork during this to help free it. Once the sample is only on the SAC fork the hook can be removed from the SAC and the “STC-SAC valve close sequence can be run.” The sample is now ready to be measured.

A.2.2 Operation of XPS

Prior to turning on the X-ray gun the vacuum level of the SAC should be checked. Normally during operation this system is around $10^{-8} – 10^{-9}$ torr. If the vacuum is bad do not turn on the gun and get help! The analyzer window should have the following parameters for standard operation, Mode: spectrum, lens: hybrid, resolution: pass energy (this varies), slot. The pass energy will determine the resolution of the sample but lower the counts: 160 should be used for survey scans and centering, 20 is often used for higher resolution, but 40 can be used to

increase the number of counts but will not resolve very close peaks. The neutralizer should be turned on unless the sample is will grounded and conducting to the sample holder.

To turn on the X-ray gun place the system in standby for a few minutes, afterwards the gun can be turned on: Standard operating is at 10 emission 15 voltage. The carbon 1s peak is often used for sample height optimization. In the acquisition window make sure you are in snap shot mode and turn on the acquisition to collect the "carbon 1s peak." In the positions table add the position to be optimized. Run the "auto z" program after clicking "grab scan", if you would like the program to do this manually you can add position, grab scan, and then change the drop down window to required and this will automatically happen during your sequence.

In the manager window sequences can be created. A general sequence is the following, (1) data set, (2) positions table, (3) survey (4) high res scans (5) loop. To add things to your program click the tabs on the right and edit the window (all very similar to the manual window). When the section is complete use the middle mouse button to add to the program.

1. Data set: load the program here you would like your data saved as. No spaces can be used in the file name or the folder names. (Good example (January2013/Solar_012113.dset).
2. Positions table: Here you can either load the current position of the table or the whole table set up previously
3. Survey: This is a low-resolution scan of all the of binding energies, good for seeing what elements are present. Usually run at 160 pass energy.
4. High res scans: Here scans are measured much longer at lower pass energy (20). The step size is between (0.05 – 0.1 eV for good resolution). Dwell time is standard at

300, sweeps are increased to iterate out noise. Very noisy samples can take up to 20 scans.

5. Loop: One minus the number of sample positions to be run. Click on loop while holding "ctrl" and click back to position to highlight both squares. Right click and press loop back to allow your program to cycle.

A.2.3 Data analysis using CasaXPS

To open files in CasaXPS please use the dumpdataset program to convert .dset files to .kal. In Casa use convert under the file menu to open to .kal file and convert to .vmas. To calibrate the scans the C 1s peak is used. Open the C 1s scan and click the "quantify" button,"under regions press create. Hold down shift and select the row of scans to be calibrated, click on the C 1s scan on the left window again to select it after this. Click the "processing" button, open the calibration tap. Energy calibration: Measured, read this position from the quantify window, true is 284.8. Click regions and components under the adjust box then click "apply to selection." If a mistake is made under the processing window and the processing history tab a summary of everything that has been done to the spectra is listed and can be undone.

To quantify peaks create a region on the spectra to be analyzed as described above. BG Type can be changed, Shirley is often used for the sloping background in XPS. Av. Width is set at 1 for default and can be increased up to 10 points. This will average the background over a number of points. Click on the components tab, and then press "create" to deconvolute the peaks. The line shape is a default voight fit, but this can be varied depending on the symmetry of the peaks. The area constraint should be used when fitting split peaks. The position and position constraint can be set here too. When the component conditions are set the "fit components" button can be pressed a number of times until the fits don't seem to be changing. The name of

each component peak should be changed in order to have the quantification give the right numbers. Percent concentration can be read directly from this window or a report can be generated. Highlight all scans to be quantified and open the "quantification" window again. In the report spec., tab click the "all" button and then "area report" to view a summary of the data.

A.3 Detailed synthesis of dip coating mesoporous thin films

At least an hour prior to dip coating films dry house air should be flow through the dip coating chamber. Additionally the oven (muffles) should be set to 80°C at this time. A general procedure for dip coating films follows:

- Right before dip coating the oven should be turned down to 60°C, it is also recommended that a foil be placed in the oven that will sit above the samples to prevent dust to falling into the samples.
- Place substrate into a solution of 3.5 g KOH, 30 mL of ultrapure water, and 5 mL of ethanol for approximately 30 sec. This process helps with substrate wetting.
- Remove substrate from cleaning solution and rinse off with ethanol, a kim wipe should be used to whip the substrates clean, careful care should be made to make sure there are now smudges on the film. Some force will be needed to get them cleaned fully.
- Any little bit of dust/dirt let on the sample should be blown off with dry air.
- A hemostat should be clipped to the top of the substrate and then secured by a binder clip. The film can then be suspended to the clip in the dip coating chamber and then lowered into the dip coating cuvette. Once the door of the chamber is closed the humidity level should be measured, if it is too high wait for the air to purge out of the chamber.
- Then sample can then be slowly pulled from the solution at a rate determined by the material. Once fully removed the sample should be given ~ 30 sec to dry.

- Once dry the sample can be carefully removed and shielded from dirt by hand on the way to the oven. The oven door should be closed gently to prevent deposition of dirt on the surface of the sample.
- A standard initial heating program from the materials discussed in this thesis is the following: ramp from 60°C to 80°C in 1 hour, hold for 6 hours, ramp to 130°C in 2 hours, hold for 8 hours, ramp to 180°C in 1 hour, the samples can be removed once they reach 180°C. At this point the samples will still be amorphous and the polymer will remain in the pores.

A.3.1 Synthetic conditions of CFO thin films

Solutions for dip coating CFO should be made approximately 3 days in advance of dip coating. The sol-gel solution is made by placing 0.31 g of iron nitrate nonahydrate, 0.11 g of cobalt nitrate hexhydrate in a vial, 1 mL each of ethanol and 2-methoxyethanol is added along with 0.04 mL of glacial acetic acid, this solution is then stirred for the 3 day period. Care must be taken to prevent the sample from heating up during this period. To do this a petri dish can be turned upside down on the stir plate being used before the sample is placed on. This synthesis is modified from previously published work.[5]

The polymer solution is made depending on the polymer being used, the PB-polymer or PEP polymer is 0.035 g in 2 mL of ethanol this solution is placed on a stir plate at ~40 – 50°C until the polymer dissolves. This should be made at least 2 hours in advance but it is better to make the polymer solution when the sol is made to insure the polymer is fully dissolved. Approximately 1 hour before dip coating the 2 solutions should be mixed and allowed to stir until dip coating. Solutions need to be filtered prior to dip coating.

Dip coating protocols described above can be used for CFO. Optimal humidity for CFO is 16% with these polymers, if the films are cloudy after initial heating the humidity was most likely too high and the samples soaked up water and cracked. Other possible explanations are too thick of films (decrease dip speed to fix this), or the dip coating process took too long allowing the samples to soak up water in the oven.

Finally crystallization of CFO can be done by taking the samples to a minimum crystallization temperature of 500°C. The ramp up the final crystallization temperature should be 10°C/min. Hotter temperatures result in larger grains and a breakdown of morphology. The PB-polymer seems to be more well suited to reach higher temperatures as it breaks down at a higher temperature.

A.4 Detailed synthesis of block co-polymer films

All solutions used for the block co-polymer films should be made the night before and allowed the mix overnight to insure the polymers are completely dissolved. All polymers can be purchased from polymer source, the brush is a hydroxy-terminated polydimethylsiloxane (PDMS-OH) with a molecular weight of 5.3 kg/mol. The block co-polymer is a symmetric poly(styrene)-b-poly(methylmethacrylate) (PS-b-PDMS) with a molecular weight of 34.0 – 11.0 kg/mol (PDI <1.1). A 1.5% (0.15g in 9.85g CCl_4) solution is used for the brush, and 0.5% (0.05g in 9.95g CCl_4) solution is used for the BCP.

A.4.1 Substrate cleaning and brush deposition

All substrates should be cleaned in a piranha bath kept at 85°C for at least 1hr. Once the samples are removed from the bath they should be rinsed with ultra pure water and then blown

dry. Careful care should be taken to avoid creating water spots on the top surface of the films. Rinsing with chloroform and ethanol can do a final cleaning of the substrates.

Spin conditions for the brush are as follows: ramp 5 sec, spin speed 3,000 rpm, dwell 20 sec. Films should be pre-wet with CCl_4 once just dry the brush solution should be pressed through a 0.45 μm PVDF syringe filter onto the surface of the film once fully covered the spin program should be started.

To graft the brush to the surface the samples should be kept in a 150°C vacuum oven over night (~16 hrs).

A.4.2 Brush removal and BCP deposition

The ungrafted brush is removed by the same rinsing procedure with ethanol and chloroform as described above when cleaning the substrate for the brush deposition. Spin coating parameters for the brush are: ramp 5 sec, spin speed 7,000 rpm, dwell 20 sec. As described above the solution must be filtered with a PVDF filter prior to deposition on the substrate.

A.4.3 Solvent annealing of BCP films

The solvents used for the annealing are a toluene:heptane mixture at a 3.5:1 ratio. Each solvent annealing chamber holds approximately 60 mL of solution so you will need 47 mL of toluene and 13 mL of heptane for each chamber. This solution should be mixed well prior to putting it in the annealing chamber. The distance from the sample to the solution can measure the volume of solution to put in the chamber. For non-patterned substrates this distance should be 1 cm, and 0.6 cm for patterned substrates. The samples should be placed in the chambers and covered with glass petri dishes for 4 hours.

A.4.4 REI conditions

The STS-AOE in the nanolab is used for the REI step. Samples should be mounted to 4-inch carrier wafers with cool grease. A drop of grease should be placed on the wafer and the sample dropped on top. The sample is then carefully moved back and forth until it is flush with the substrate and well secured. No extra grease should squeeze out from underneath the substrate. Cool grease can be cleaned off with acetone but this solvent will dissolve the BCP so extra care should be taken when cleaning the films.

Prior to processing a sample wafer an O_2 clean process should be run. Insert a clean silicon wafer into the instrument and run a 30 min cleaning cycle. The program "O2 clean" is automated. This should be done first whenever the instrument is used.

To run the process in automatic mode the program 'BCPRAF' should be selected. Click batch and enter 2 if a second wafer needs to be run. To run the process manually, after the pump down of the anti-chamber check that the slot selected is the correct wafer. Press 'load' once the icon becomes ready. In the manual window, click 'select' to load the proper sequence, and select process to start the program. The recipes should be run, BCP_CF4 and then BCP_O2 if running manually. BCP_CF4, should be run for 35 sec, BCP_O2 is a 25 sec process. If etching doesn't seem complete these values may need to be increased/decreased in the future.

BCP_CF4: Base pressure 1.0 mTorr, gas flow, O2 8.0, 5%, CF4 30.0, 5%, ICP power 0, RIE power 100.

BCP_O2: Base pressure 1.0 mTorr, gas flow, O2 40.0, 5%, ICP power 0, RIE power 100.

REFERENCES

1. Parkin, S. S. P. *et al.* Exchange-biased magnetic tunnel junctions and application to nonvolatile magnetic random access memory (invited). *J. Appl. Phys.* **85,** 5828 (1999).

2. Kryder, M. H. *et al.* Heat Assited Magnetic Recording. *Magn. IEEE* **96,** 1810–1835 (2008).

3. Wu, T. *et al.* Electrical control of reversible and permanent magnetization reorientation for magnetoelectric memory devices. *Appl. Phys. Lett.* **98,** 262504 (2011).

4. Curie, P. Sur la symétrie dans les phénomènes physiques, symétrie d"un champ électrique et d"un champ magnétique. *J. Phys. Théorique Appliquée* **3,** 393–415 (1894).

5. Quickel, T. E., Le, V. H., Brezesinski, T. & Tolbert, S. H. On the correlation between nanoscale structure and magnetic properties in ordered mesoporous cobalt ferrite (CoFe2O4) thin films. *Nano Lett.* **10,** 2982–8 (2010).

6. Wu, T. *et al.* Domain engineered switchable strain states in ferroelectric (011) [Pb(Mg1/3Nb2/3)O3](1−x)-[PbTiO3]x (PMN-PT, x≈0.32) single crystals. *J. Appl. Phys.* **109,** 124101 (2011).

7. Bur, A. *et al.* Strain-induced magnetization change in patterned ferromagnetic nickel nanostructures. *J. Appl. Phys.* **109,** 123903 (2011).

8. Spaldin, N. a & Fiebig, M. Materials science. The renaissance of magnetoelectric multiferroics. *Science* **309,** 391–2 (2005).

9. Kimura, T. *et al.* Magnetic control of ferroelectric polarization. *Nature* **426,** 55–8 (2003).

10. Dzyaloshinsky, I. A Thermodynamic Theory of " weak " Ferromagnetism of Antiferromagnetics. *J. Phys. Chem. Solids* **4,** 241–255 (1958).

11. Moriya, T. New Mechanism of Anisotropic Superexchange Interaction. *Phys. Rev. Lett.* **4,** 228–230 (1960).

12. Moriya, T. Anisotropic Superexchange Interaction and Weak Ferromagnetism. *Phys. Rev.* **120,** 91–98 (1960).

13. Kimura, T. Magnetoelectric Hexaferrites. *Annu. Rev. Condens. Matter Phys.* **3,** 93–110 (2012).

14. Kitagawa, Y. *et al.* Low-field magnetoelectric effect at room temperature. *Nat. Mater.* **9,** 797–802 (2010).

15. Spaldin, N. A. *Magnetic Materials: Fundamentals and Device Applications*. (Cambridge University Press, 2003).

16. Prinz, G. A. Magnetoelectronics. *Science (80-.).* **282,** 1660–1663 (1998).

17. Binasch, G., Grunberg, P., Saurenbach, F. & Zinn, W. Enhanced Magnetoresistance in Layered Magnetic-Structures with Antiferromagnetic Interlayer Exchange. *Phys. Rev. B* **39,** 4828–4830 (1989).

18. Tsymbal, E. Y. & Pettifor, D. G. in *Solid State Physics, Vol 56* **56,** 113–237 (Elsevier Academic Press Inc, 2001).

19. Johnson, M. Spintronics. *J. Phys. Chem. B* **109,** 14278–14291 (2005).

20. Kent, a. D., Özyilmaz, B. & del Barco, E. Spin-transfer-induced precessional magnetization reversal. *Appl. Phys. Lett.* **84,** 3897 (2004).

21. Papusoi, C. *et al.* 100 Ps Precessional Spin-Transfer Switching of a Planar Magnetic Random Access Memory Cell With Perpendicular Spin Polarizer. *Appl. Phys. Lett.* **95,** 072506 (2009).

22. Houssameddine, D. *et al.* Spin-torque oscillator using a perpendicular polarizer and a planar free layer. *Nat. Mater.* **6,** 441–7 (2007).

23. Lee, K. J., Redon, O. & Dieny, B. Analytical investigation of spin-transfer dynamics using a perpendicular-to-plane polarizer. *Appl. Phys. Lett.* **86,** 022505 (2005).

24. Ebels, U. *et al.* Macrospin description of the perpendicular polarizer-planar free-layer spin-torque oscillator. *Phys. Rev. B* **78,** 024436 (2008).

25. Seki, T., Mitani, S., Yakushiji, K. & Takanashi, K. Magnetization reversal by spin-transfer torque in 90° configuration with a perpendicular spin polarizer. *Appl. Phys. Lett.* **89,** 172504 (2006).

26. Blondel, A., Meier, J. P., Doudin, B. & Ansermet, J. Giant magnetoresistance of nanowires of multilayers. *Appl. Phys. Lett.* **65,** 3019–3021 (1994).

27. Piraux, L. *et al.* Giant magnetoresistance in magnetic multilayered nanowires. *Appl. Phys. Lett.* **65,** 2484 (1994).

28. Liu, K., Nagodawithana, K., Searson, P. C. & Chien, C. L. Perpendicular giant magnetoresistance of multilayered Co/Cu nanowires. *Phys. Rev.* **51,** 7381–7385 (1995).

29. Martin, C. R. Nanomaterials: A Membrane-Based Synthetic Approach. *Science (80-.).* **266,** 1961–1966 (1994).

30. Routkevitch, D., Bigioni, T., Moskovits, M. & Xu, J. M. Electrochemical Fabrication of CdS Nanowire Arrays in Porous Anodic ALuminum Oxide. *J. Phys. Chem.* **100,** 14037–14047 (1996).

31. Hurst, S. J., Payne, E. K., Qin, L. & Mirkin, C. A. Multisegmented One-Dimensional Nanorods Prepared by Hard-Template Synthetic Methods. *Angew. Chem. Int. Ed.* **45,** 2672–2692 (2006).

32. Banholzer, M. J., Qin, L., Millstone, J. E., Osberg, K. D. & Mirkin, C. A. On-wire lithography: synthesis, encoding and biological applications. *Nat. Protoc.* **4,** 838–848 (2009).

33. Chen, M. *et al.* Tuning the response of magnetic suspensions. *Appl. Phys. Lett.* **82,** 3310–3312 (2003).

34. Liang, H.-P. *et al.* Ni−Pt Multilayered Nanowire Arrays with Enhanced Coercivity and High Remanence Ratio. *Inorg. Chem.* **44,** 3013–3015 (2005).

35. Chen, M., Searson, P. C. & Chien, C. L. Micromagnetic behavior of electrodeposited Ni/Cu multilayer nanowires. *J. Appl. Phys.* **93,** 8253–8255 (2003).

36. Chen, M., Chien, C.-L. & Searson, P. C. Potential Modulated Multilayer Deposition of Multisegment Cu/Ni Nanowires with Tunable Magnetic Properties. *Chem. Mater.* **18,** 1595–1601 (2006).

37. Darling, S. B. Directing the self-assembly of block copolymers. *Prog. Polym. Sci.* **32,** 1152–1204 (2007).

38. Kim, H.-C., Park, S.-M. & Hinsberg, W. D. Block copolymer based nanostructures: materials, processes, and applications to electronics. *Chem. Rev.* **110,** 146–77 (2010).

39. Black, C. T. *et al.* Polymer self assembly in semiconductor microelectronics. *IBM J. Res Dev.* **51,** 605–633 (2007).

40. Park, M., Harrison, C., Chaikin, P. M., Register, R. A. & Adamson, D. H. Block Copolymer Lithography: Periodic Arrays of 1011 Holes in 1 Square Centimeter. *Science (80-.).* **276,** 1401–1404 (1997).

41. Thurn-Albrecht, T. *et al.* Ultrahigh-Density Nanowire Arrays Grown in Self-Assembled Diblock Copolymer Templates. *Science (80-.).* **290,** 2126–2129 (2000).

42. Segalman, R. a., Yokoyama, H. & Kramer, E. J. Graphoepitaxy of Spherical Domain Block Copolymer Films. *Adv. Mater.* **13,** 1152–1155 (2001).

43. Ludwigs, S. *et al.* Self-assembly of functional nanostructures from ABC triblock copolymers. *Nat. Mater.* **2,** 744–7 (2003).

44. Kim, S. O. *et al.* Epitaxial self-assembly of block copolymers on lithographically defined nanopatterned substrates. *Nature* **424,** 411–4 (2003).

45. Stoykovich, M. P. *et al.* Directed assembly of block copolymer blends into nonregular device-oriented structures. *Science* **308,** 1442–6 (2005).

46. Chai, J., Wang, D., Fan, X. & Buriak, J. M. Assembly of aligned linear metallic patterns on silicon. *Nat. Nanotechnol.* **2,** 500–6 (2007).

47. Tang, C., Lennon, E. M., Fredrickson, G. H., Kramer, E. J. & Hawker, C. J. Evolution of Block Copolymer Lithography to Highly Ordered Square Arrays. *Science (80-.).* **322,** 429–432 (2008).

48. Park, S. *et al.* Square-Inch Arrays from Block Copolymers with Lateral Order. *Science (80-.).* **323,** 1030–1033 (2009).

49. Jeong, S.-J. *et al.* Universal Block Copolymer Lithography for Metals, Semiconductors, Ceramics, and Polymers. *Adv. Mater.* **20,** 1898–1904 (2008).

50. Kim, S. O. *et al.* Novel Complex Nanostructure from Directed Assembly of Block Copolymers on Incommensurate Surface Patterns. *Adv. Mater.* **19,** 3271–3275 (2007).

51. Ruiz, R. *et al.* Density multiplication and improved lithography by directed block copolymer assembly. *Science* **321,** 936–9 (2008).

52. Bita, I. *et al.* Graphoepitaxy of self-assembled block copolymers on two-dimensional periodic patterned templates. *Science* **321,** 939–43 (2008).

53. Jeong, S.-J. *et al.* Soft graphoepitaxy of block copolymer assembly with disposable photoresist confinement. *Nano Lett.* **9,** 2300–5 (2009).

54. Cheng, J. Y. *et al.* Simple and versatile methods to integrate directed self-assembly with optical lithography using a polarity-switched photoresist. *ACS Nano* **4,** 4815–23 (2010).

55. Cheng, J. Y., Ross, C. a., Thomas, E. L., Smith, H. I. & Vancso, G. J. Templated Self-Assembly of Block Copolymers: Effect of Substrate Topography. *Adv. Mater.* **15,** 1599–1602 (2003).

56. Cheng, J. Y., Mayes, A. M. & Ross, C. a. Nanostructure engineering by templated self-assembly of block copolymers. *Nat. Mater.* **3,** 823–8 (2004).

57. Park, S.-M. *et al.* Directed Assembly of Lamellae- Forming Block Copolymers by Using Chemically and Topographically Patterned Substrates. *Adv. Mater.* **19,** 607–611 (2007).

58. Sun, S. Recent Advances in Chemical Synthesis, Self-Assembly, and Applications of FePt Nanoparticles. *Adv. Mater.* **18,** 393–403 (2006).

59. Chen, M. *et al.* Patterning self-assembled FePt nanoparticles. *J. Magn. Magn. Mater.* **266,** 8–11 (2003).

60. Benkoski, J. J. *et al.* Dipolar organization and magnetic actuation of flagella-like nanoparticle assemblies. *J. Mater. Chem.* **21,** 7314 (2011).

61. Kim, B. Y., Shim, I.-B., Monti, O. L. a & Pyun, J. Magnetic self-assembly of gold nanoparticle chains using dipolar core-shell colloids. *Chem. Commun.* **47,** 890–2 (2011).

62. Sun, S., Murray, C. B., Weller, D., Folks, L. & Moser, A. Monodisperse FePt Nanoparticles and Ferromagnetic FePt Nanocrystal Superlattices. *Science (80-.).* **287,** 1989–1992 (2000).

63. Xu, K., Qin, L. & Heath, J. R. The crossover from two dimensions to one dimension in granular electronic materials. *Nat. Nanotechnol.* **4,** 368–372 (2009).

64. Sharma, N., Jaffari, G. H., Shah, S. I. & Pochan, D. J. Orientation-dependent magnetic behavior in aligned nanoparticle arrays constructed by coaxial electrospinning. *Nanotechnology* **21,** 85707 (2010).

65. Zhang, L. & Manthiram, a. Experimental study of ferromagnetic chains composed of nanosize Fe spheres. *Phys. Rev. B. Condens. Matter* **54,** 3462–3467 (1996).

66. Chou, S. Y., Wei, M. S., Krauss, P. R. & Fischer, P. B. Single-domain magnetic pillar array of 35 nm diameter and 65 Gbits/in.2 density for ultrahigh density quantum magnetic storage. *J. Appl. Phys.* **76,** 6673 (1994).

67. Ross, C. a. *et al.* Fabrication of patterned media for high density magnetic storage. *J. Vac. Sci. Technol. B Microelectron. Nanom. Struct.* **17,** 3168 (1999).

68. Morin, S. a *et al.* Assembly of nanocrystal arrays by block-copolymer-directed nucleation. *Angew. Chemie* **48,** 2135–9 (2009).

69. Haryono, A. & Binder, W. H. Controlled arrangement of nanoparticle arrays in block-copolymer domains. *Small* **2,** 600–611 (2006).

70. Darling, S. B., Yufa, N. a., Cisse, a. L., Bader, S. D. & Sibener, S. J. Self-Organization of FePt Nanoparticles on Photochemically Modified Diblock Copolymer Templates. *Adv. Mater.* **17,** 2446–2450 (2005).

71. Darling, S. B. & Bader, S. D. A materials chemistry perspective on nanomagnetism. *J. Mater. Chem.* **15,** 4189 (2005).

72. Gutfleisch, O., Lyubina, J., Mller, K.-H. & Schultz, L. FePt Hard Magnets. *Adv. Eng. Mater.* **7,** 208–212 (2005).

73. Dai, Z. R., Sun, S. & Wang, Z. L. Phase Transformation , Coalescence , and Twinning of Monodisperse FePt Nanocrystals. *Nano Lett.* **1,** 443–447 (2001).

74. Bae, S.-Y., Shin, K.-H., Jeong, J.-Y. & Kim, J.-G. Feasibility of FePt longitudinal recording media for ultrahigh density recording. *J. Appl. Phys.* **87,** 6953 (2000).

75. Delalande, M. *et al.* L 1 0 Ordering of Ultrasmall FePt Nanoparticles Revealed by TEM In Situ Annealing. *J. Phys. C Solid State Phys.* **116,** 6866–6872 (2012).

76. Moser, A. *et al.* Magnetic recording : advancing into the future. *J. Phys. D. Appl. Phys.* **35,** R157–R167 (2002).

77. Frey, N. a, Peng, S., Cheng, K. & Sun, S. Magnetic nanoparticles: synthesis, functionalization, and applications in bioimaging and magnetic energy storage. *Chem. Soc. Rev.* **38,** 2532–42 (2009).

78. Andreozzi, a *et al.* The fabrication of tunable nanoporous oxide surfaces by block copolymer lithography and atomic layer deposition. *Nanotechnology* **22,** 335303 (2011).

79. Peng, Q., Tseng, Y.-C., Darling, S. B. & Elam, J. W. Nanoscopic patterned materials with tunable dimensions via atomic layer deposition on block copolymers. *Adv. Mater.* **22,** 5129–33 (2010).

80. Kim, J., Rong, C., Lee, Y., Liu, J. P. & Sun, S. From Core / Shell Structured FePt / Fe 3 O 4 / MgO to Ferromagnetic FePt Nanoparticles. *Chem. Mater.* **20,** 7242–7245 (2008).

81. Kim, J., Rong, C., Liu, J. P. & Sun, S. Dispersible Ferromagnetic FePt Nanoparticles. *Adv. Mater.* **21,** 906–909 (2009).

82. Catalan, G. & Scott, J. F. Physics and Applications of Bismuth Ferrite. *Adv. Mater.* **21,** 2463–2485 (2009).

83. Scott, J. F. Multiferroic memories. *Nat. Mater.* **6,** 256–257 (2007).

84. Ederer, C. & Spaldin, N. Weak ferromagnetism and magnetoelectric coupling in bismuth ferrite. *Phys. Rev. B* **71,** 060401 (2005).

85. Ederer, C. & Spaldin, N. Influence of strain and oxygen vacancies on the magnetoelectric properties of multiferroic bismuth ferrite. *Phys. Rev. B* **71,** 224103–224109 (2005).

86. Wang, J. *et al.* Epitaxial BiFeO3 multiferroic thin film heterostructures. *Science* **299,** 1719–22 (2003).

87. Lee, J. H. *et al.* A strong ferroelectric ferromagnet created by means of spin-lattice coupling. *Nature* **466,** 954–8 (2010).

88. He, Q. *et al.* Electrically controllable spontaneous magnetism in nanoscale mixed phase multiferroics. *Nat. Commun.* **2,** 225 (2011).

89. Teague, J. R., Gerson, R. & James, W. J. Dielectric Hystersis in Single Crystal BiFeO3. *Solid State Commun.* **8,** 1073–1074 (1970).

90. Sosnowska, I., Peterlin-Neumaier, T. & Steichele, E. Spiral magnetic ordering in bismuth ferrite. *J. Phys. C Solid State Phys.* **15,** 4835–4846 (1982).

91. Wang, J. *et al.* Response to Comment on "Epitaxial BiFeO3 Multiferroic Thin Film Heterostructures."*Science (80-.).* **307,** 1203b–1203b (2005).

92. Eerenstein, W. *et al.* Comment on "Epitaxial BiFeO3 multiferroic thin film heterostructures". *Science* **307,** 1203; author reply 1203 (2005).

93. Hatt, A. J. & Spaldin, N. a. Strain-induced isosymmetric phase transition in BiFeO_{3}. *Phys. Rev. B* **81,** 1–5 (2010).

94. Ederer, C. & Spaldin, N. Effect of Epitaxial Strain on the Spontaneous Polarization of Thin Film Ferroelectrics. *Phys. Rev. Lett.* **95,** 257601 (2005).

95. Brinker, C. J., Lu, Y., Sellinger, A. & Fan, H. Evaporation-Induced Self-Assembly: Nanostructures Made Easy. *Adv. Mater.* **11,** 579–585 (1999).

96. Zhao, T. *et al.* Electrical control of antiferromagnetic domains in multiferroic BiFeO3 films at room temperature. *Nat. Mater.* **5,** 823–9 (2006).

97. Ren, S. & Wuttig, M. Spinodally synthesized magnetoelectric. *Appl. Phys. Lett.* **91,** 083501 (2007).

98. Zheng, H. *et al.* Multiferroic BaTiO3-CoFe2O4 Nanostructures. *Science* **303,** 661–3 (2004).

99. Nogués, J. & Schuller, I. K. Exchange bias. *J. Magn. Magn. Mater.* **192,** 203–232 (1999).

100. Ramesh, R. & Spaldin, N. a. Multiferroics: progress and prospects in thin films. *Nat. Mater.* **6,** 21–9 (2007).

101. Ampere, A.-M. Sur les effets des courants électriques. *Ann. Chim. Phys.* **15,** 170–218 (1820).

102. Van Suchtelen, J. Product Properties: a new application of composite materials. *Phillips Res. Rep.* **27,** 28–37 (1972).

103. Ryu, J., Priya, S., Uchino, K. & Kim, H. Magnetoelectric effect in composites of magnetostrictive and piezoelectric materials. *J. Electroceramics* **8,** 107–119 (2002).

104. Ortega, N., Kumar, A., Katiyar, R. S. & Rinaldi, C. Investigation of temperature-dependent polarization, dielectric, and magnetization behavior of multiferroic layered nanostructure. *Thin Solid Films* **519,** 641–649 (2010).

105. Wan, J. G., Liu, J.-M., Wang, G. H. & Nan, C. W. Electric-field-induced magnetization in Pb(Zr,Ti)O[sub 3]/Terfenol-D composite structures. *Appl. Phys. Lett.* **88,** 182502 (2006).

106. Chung, T.-K., Carman, G. P. & Mohanchandra, K. P. Reversible magnetic domain-wall motion under an electric field in a magnetoelectric thin film. *Appl. Phys. Lett.* **92,** 112509 (2008).

107. Murakami, M. *et al.* Tunable multiferroic properties in nanocomposite PbTiO[sub 3]–CoFe[sub 2]O[sub 4] epitaxial thin films. *Appl. Phys. Lett.* **87,** 112901 (2005).

108. Yamasaki, Y. *et al.* Magnetic Reversal of the Ferroelectric Polarization in a Multiferroic Spinel Oxide. *Phys. Rev. Lett.* **96,** 207204 (2006).

109. Yang, J. J. *et al.* Electric field manipulation of magnetization at room temperature in multiferroic CoFe[sub 2]O[sub 4]/Pb(Mg[sub 1/3]Nb[sub 2/3])[sub 0.7]Ti[sub 0.3]O[sub 3] heterostructures. *Appl. Phys. Lett.* **94,** 212504 (2009).

110. Chu, Y.-H. *et al.* Electric-field control of local ferromagnetism using a magnetoelectric multiferroic. *Nat. Mater.* **7,** 478–82 (2008).

111. Chung, T.-K., Keller, S. & Carman, G. P. Electric-field-induced reversible magnetic single-domain evolution in a magnetoelectric thin film. *Appl. Phys. Lett.* **94,** 132501 (2009).

112. Bean, C. & Livingston, J. D. Superparamagnetism. *J. Appl. Phys.* **30,** S120–S129 (1959).

113. Leslie-Pelecky, D. L. & Rieke, D. R. Magnetic properties of nanostructured materials. *Chem. Mater.* **8,** 1770–1783 (1996).

114. Cowburn, R. P. Superparamagnetism and the future of magnetic random access memory. *J. Appl. Phys.* **93,** 9310 (2003).

115. Chen, Y., Peng, D.-L., Lin, D. & Luo, X. Preparation and magnetic properties of nickel nanoparticles via the thermal decomposition of nickel organometallic precursor in alkylamines. *Nanotechnology* **18,** 505703 (2007).

116. Shevchenko, E. V, Talapin, D. V, Murray, C. B. & O'Brien, S. Structural characterization of self-assembled multifunctional binary nanoparticle superlattices. *J. Am. Chem. Soc.* **128,** 3620–37 (2006).

117. Weiler, M. *et al.* Voltage controlled inversion of magnetic anisotropy in a ferromagnetic thin film at room temperature. *New J. Phys.* **11,** 013021 (2009).

118. Hansen, M. F. & Mørup, S. Estimation of blocking temperatures from ZFC/FC curves. *J. Magn. Magn. Mater.* **203,** 214–216 (1999).

119. Knobel, M. *et al.* Superparamagnetism and Other Magnetic Features in Granular Materials: A Review on Ideal and Real Systems. *J. Nanosci. Nanotechnol.* **8,** 2836–2857 (2008).

120. Yoon, M. *et al.* Superparamagnetic properties of nickel nanoparticles in an ion-exchange polymer film. *Mater. Chem. Phys.* **91,** 104–107 (2005).

121. Hu, J.-M., Li, Z., Wang, J. & Nan, C. W. Electric-field control of strain-mediated magnetoelectric random access memory. *J. Appl. Phys.* **107,** 093912 (2010).

122. Lee, K. & Kang, S. H. Development of Embedded STT-MRAM for Mobile System-on-Chips. *IEEE Trans. Magn.* **47,** 131–136 (2011).

123. Lee, K. & Kang, S. H. Design Consideration of Magnetic Tunnel Junctions for Reliable High-Temperature Operation of STT-MRAM. *IEEE Trans. Magn.* **46,** 1537–1540 (2010).

124. Skumryev, V. *et al.* Beating the superparamagnetic limit with exchange bias. *Nature* **423,** 850–853 (2003).